2017 NA62 Status Report to the CERN SPSC

Abstract

The status of the analysis of the data collected in 2016 by the NA62 experiment is reported. About 5×10^{11} K^+ decays have been taken to study the $K^+ \to \pi^+ \nu \bar{\nu}$ decay. Preliminary results from the $K^+ \to \pi^+ \nu \bar{\nu}$ analysis based on about 5% of the 2016 statistics are summarised in this document. Analysis on exotic physics searches and rare and forbidden decays are also discussed.

Contents

1   Introduction

This NA62 2017 report to the SPSC emphasizes the status of the analysis. The overall, very important message is that in 2016 the first set of "$\pi\nu\nu$ quality data" has been collected, the experiment has been completely commissioned and the preparations for the 2017 run are all underway as planned. We mention that several unexpected problems were detected during the last year and solved, the last one being the high voltage (HV) sparks observed in the LKr calorimeter. These sparks were finally explained by the discovery of a leak of Kr which developed over the years to the point that some high HV electrodes were left exposed to the Kr gas leading to discharges. The leak was sealed and appropriate steps are being taken to refill the calorimeter with the required amount of LKr to run in stable conditions. Detector-wise the highlight of the 2016 run was the running of the complete Gigatracker (GTK) without noise and including three fully functioning stations. Another important step was the deployment of the complete Level 1 software trigger including the algorithm using the straw chambers.

In 2016 data taking was mostly performed at 40% of the nominal intensity, limited by the quality of the SPS slow extraction. The quality of the slow extraction is expected to improve in 2017 and if this confirmed, NA62 will be able to run at higher intensities, typically 2/3 of nominal or $20 - 25 \times 10^{11}$ protons on the target T10. We shall insist that at this stage of the experiment stable data taking and good data quality and efficiency are preferable to taking data at the ultimate sustainable rate. This is especially true because the $K^+ \to \pi^+\nu\bar{\nu}$ analysis is sensitive to GTK mis-matching which depends on the instantaneous beam rate.

The document is structured as follows: Sections 2 provides an overview of the 2016 NA62 layout; Sections 3 and 4 describe the triggers used in 2016 and present a summary of the data collected in 2016, respectively; Section 5 gives a description of the offline detector reconstructions; Section 6 gives an overview of the data analysis; Section 7 reports the status of the $K^+ \to \pi^+\nu\bar{\nu}$ analysis while Sections 8 and 9 report the status of the analysis on exotic searches and rare and forbidden decays, respectively. Finally the status of the NA62 and NA48/2 publications is presented in Section 10.

2   Detector Description

Figure 1 shows the layout of the apparatus. Primary protons from the SPS (400 GeV/c) strike a 40 cm long Be target (T10) from which a secondary hadron beam of 75 GeV/c (momentum bite 1%) is selected and transported to the decay region. For the detailed descriptions of the detectors used in the analysis the reader is referred to the NA62 detector paper [1]. The incoming kaon is positively identified by a differential Cherenkov counter (KTAG) and its momentum and direction are measured by three stations of Si pixel detectors (GTK) capable of 100 ps time resolution. The kaon fraction of the beam is approximately 6%. Inelastic interactions in the downstream station of the GTK are vetoed by the CHANTI anticounter. The decay tank is surrounded by 12 stations of large angle vetoes (LAV) and the pion is measured by four stations of straw trackers (STRAW), two upstream and two downstream of the dipole magnet MNP33 (p_t kick of 270 MeV/c). Timing and pion-muon separation are provided by the RICH, while plastic scintillators (NA48-CHOD and CHOD) are used for triggering, pattern recognition
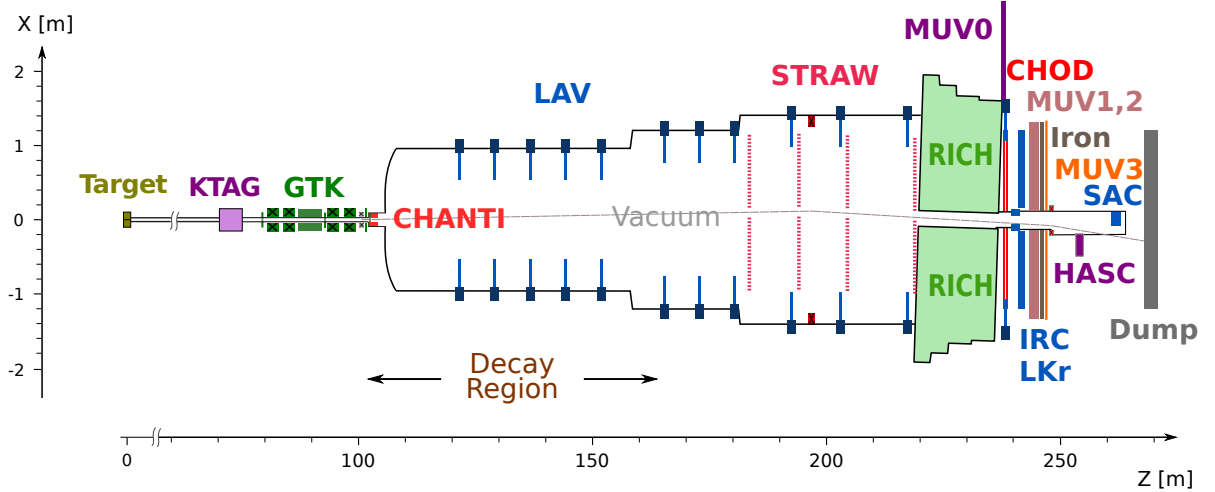
Figure 1: Schematic layout of the NA62 experiment in the xz plane.

and timing. Photon rejection in the forward region is provided by the liquid krypton calorimeter (LKr), an intermediate ring calorimeter (IRC) and a small angle calorimeter (SAC). Hadron calorimeters (MUV1 and MUV2) and plastic scintillator detectors (MUV0 and MUV3) are used to suppress muons while particles in the beam region are deflected by a sweeping magnet. A hadron calorimeter (HASC) placed laterally to the beam pipe between the last sweeping magnet and the SAC detects π^+ from K^+ decays traveling along the beam. The T10 target is the origin of the NA62 reference frame system; the z axis is directed along the detector axis, oriented from T10 towards the dump; the y axis is directed upwards and the x axis is oriented to form a right-handed reference system.

3 Trigger

A two-level trigger architecture is used for data taking. Level 0 (L0) signals ("primitives") are generated by individual detectors and sent to a L0 trigger processor (L0TP). L0TP combines the primitives and provides L0 trigger decisions; depending on the L0 trigger, detectors send data to the NA62 PC-Farm. The PC-Farm assembles the events and runs Level 1 (L1) software trigger algorithms to reduce data further before finally being stored on disk.

3.1 Level 0

The principal L0 primitives used during most of the 2016 data taking are the following. The L0TP logic is based on coincidences of these signals within a 12.5 ns wide time window.

- The RICH condition approximately corresponds to a coincidence of signals in at least three RICH photomultipliers (PMT) (typically in a 25 ns time window). It forms the basis of all physics triggers and provides the trigger time.

- The Q_1, Q_2 and Q_X conditions correspond to a signal in any CHOD tile, coincidences of signals in at least two quadrants and in opposite quadrants (typically in a 10 ns

time window), respectively.

- The M1 and M2 conditions correspond to a signal in any MUV3 tile and a coincidence of signals in at least two tiles (typically in a 10 ns time window), respectively. The MO1 and MO2 conditions are similar considering the outer MUV3 tiles only; the excluded eight inner tiles account for about half of the M1 rate (mainly due to the contribution from beam pion decays).

- The LKr20 condition corresponds to the total energy deposit of at least 20 GeV in the LKr calorimeter.

- The LAV12 condition corresponds to the presence of in-time signals corresponding to the low and high discrimination thresholds in the same LAV12 counter.

- Finally, the CHOD condition is a coincidence of signals in at least two counters of the NA48-CHOD (typically in a 25 ns time window). It is used as a control trigger independent of the physics triggers. Its rate is artificially reduced ("downscaled") by a large factor.

3.2 Level 1

The following L1 software trigger algorithms were used within the 2016 data taking to select $K^+ \to \pi^+ \nu \bar{\nu}$ events and other physics channels of interest.

- The KTAG trigger uses the KTAG sector-multiplicity to positively identify a beam kaon and reject accidental L0 triggers. The event selection requires a minimum of five out of eight KTAG sectors in coincidence and in time with the L0 trigger.

- The LAV trigger uses a hit-multiplicity cut in the twelve LAV stations aiming at reduction of the $K^+ \to \pi^+ \pi^0$ background by identifying photons emitted at large angles. The event selection requires no more than two hits in the whole LAV station system in time with the L0 trigger.

- The STRAW trigger aims at the rejection of multi-track events and one-track events reconstructed either outside the fiducial decay region or outside the track momentum range required in the $K^+ \to \pi^+ \nu \bar{\nu}$ event selection. The trigger algorithm reconstructs particle tracks by performing a two-dimensional Hough transform and a crude momentum evaluation. The following requirements are applied: 1) track momentum p smaller than $50 \, \text{GeV}/c$; 2) track closest distance of approach (CDA) to the beam axis smaller than $200 \, \text{mm}$; 3) vertex longitudinal position at the CDA smaller than $180 \, \text{m}$, i.e upstream of straw chamber 1. To minimise the reconstruction of fake tracks, a minimal p of $3 \, \text{GeV}/c$ is required and the absolute values of the track slopes in the xz and yz planes are required to be both smaller than $20 \, \text{mrad}$. Multi-track events are identified by the reconstruction of a pair of tracks with a CDA smaller than $30 \, \text{mm}$.

- The STRAW "Exotic" trigger aims to positively identifying decay channels with a negatively charged particle in the final state. The trigger algorithm uses the same particle track reconstruction of the STRAW trigger, while adding the extra requirement of negative charge for at least one of the reconstructed tracks.

6

Table 1: Level 0 trigger definition in sample A. PNN is the acronym of the trigger condition used for $K^+ \to \pi^+ \nu \bar{\nu}$. Number of triggers per spill in the 3rd column are typical counts at 40% nominal intensity before applying the downscaling factors. Downscaling factors are those typically used, with some variations along sample A.

Name	Condition	Trig/Spill	Downscaling
PNN	RICH*Q1*!Q_X*!M1*!LAV12*!LKr20	1.2 M	1
Di-muon	RICH*Q_X*MO2	0.2 M	1
Di-muon exotic	RICH*Q_2*!LKr20	0.1 M	1
Electron multi-track	RICH*Q_X*LKr20	0.7 M	2
Muon multi-track	RICH*Q_X*M1	0.5 M	5
Muon exotic	RICH*Q_2*MO1	1.4 M	10
Multi-track	RICH*Q_X	2.3 M	50
Non-muon	RICH*Q_1*!M1	4.0 M	200
Control	CHOD	6.7 M	400

The KTAG, LAV and STRAW trigger were applied sequentially on top of each other to select $K^+ \to \pi^+ \nu \bar{\nu}$ events. The trigger configuration corresponds to the condition KTAG×!LAV×STRAW and is referred to within the text as L1 PNN trigger. The STRAW "Exotics" was used within other trigger lines for decays with multiple tracks in the final state.

Typically about 200×10^3 trigger per spill were written on disk at 40% nominal intensity after L1.

4   2016 Data Samples

The 2016 run is divided into several data samples, defined depending on the status of the detectors and trigger systems. The main physics sample ("sample A") was taken at 40% nominal beam intensity, starting from the 16th of September, when the complete GTK was operational, until the 3rd of November, when high-intensity tests were performed and the KTAG emptied. This sample contains 1.1×10^5 SPS spills corresponding to about 5×10^{11} kaon decays in a 60 m long fiducial volume (Figure 2) and is composed of a mixture of all the physics triggers presented in Table 1. Sample A has been fully reprocessed and the results of the ongoing analyses reported in this document are based on sub-samples from it. The high-intensity period A+, in which the beam intensity spanned from 60% to 80% of the nominal, was collected from the 3rd to the 13th of November, mostly for rate tests. Data sample (B) collected between the 23th of July, when the complete Level 1 software trigger including the algorithm using the straw chambers became operational, and the 13th of September, is of approximately the same volume as sample A and is suitable for rare and forbidden kaon decay studies. Data sample (C) taken before the 23rd of July, with low beam intensity, will be assessed for physics studies at a later stage.
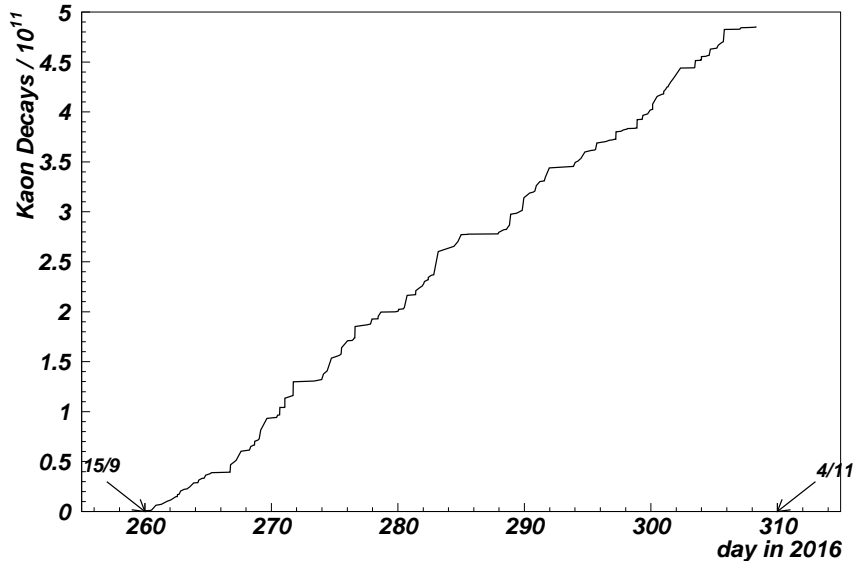
Figure 2: Integrated number of kaon decays in the 60 m long fiducial volume collected in sample A, obtained from reconstructed $K^+ \rightarrow \pi^+\pi^+\pi^-$ decays in the control trigger stream.

5 Detector Reconstruction

5.1 KTAG

KTAG channels are aligned in time and corrected for slewing; hits in different sectors are clustered iteratively in time within ± 2.5 ns around the average cluster time itself to form signal candidates; a kaon is defined as a candidate where at least 5 sectors out of 8 had at least one PMT signal; about 20 hits on average form a K^+ signal; time resolution is measured to be 70 ps RMS and the efficiency greater than 99%. In the last three weeks of the 2016 run, one sixth of the channels were not readable due to readout problems; consequently the kaon efficiency and the time resolution are measured to be 97.5% and 80 ps (RMS), respectively.

5.2 GTK

GTK stations are aligned in space with precision better than 100 μm by means of samples of $K^+ \rightarrow \pi^+\pi^+\pi^-$ decays reconstructed kinematically using tracks from the STRAW. The same $K^+ \rightarrow \pi^+\pi^+\pi^-$ sample also provides a measurement of the average and RMS of beam momentum and direction. GTK pixels are aligned in time with respect to the KTAG and time is corrected for slewing; hits in GTK are grouped in time within ± 2 ns with respect to a reference time and in space by selecting hits in different stations along directions compatible with beam particle trajectories allowed by the beam acceptance. The $K^+ \rightarrow \pi^+\nu\bar{\nu}$ analysis described below uses the time from the KTAG as reference, unless specified otherwise. A linear least squared fit provides the measurement of the track slope in the xz plane, with the position of the hits in the last station corrected for the kick induced by the Trim 5 magnet and measured from $K^+ \rightarrow \pi^+\pi^+\pi^-$; the momentum and

the slope of the track in the yz plane are computed analytically assuming the nominal value for the magnetic fields of the achromat dipoles. Corrections to measured slopes and momentum at the level of per-mille are eventually applied by comparing the corresponding measurements from $K^+ \to \pi^+\pi^+\pi^-$.

5.3 CHANTI

CHANTI channels are aligned in time with respect to the KTAG. The single channel time resolution is 1.3 ns. A candidate is defined as a set of scintillator bars belonging to the same station and hit at the same time: the bars of a candidate have to be adjacent (crossing) if they belong to the same (different) view (X or Y). The time resolution of a CHANTI candidate is 900 ps. The efficiency to detect minimum ionizing particles (MIP) is above 99% for a single view in a single station.

5.4 STRAW

Tracks are reconstructed in STRAW using the average time of the NA48-CHOD hits recorded within 25 ns from the trigger time as a reference for the measurement of the drift time in the straws; a GARFIELD [2] simulation is used to convert the drift time into the distance R of a particle trajectory from the anode wire of a hit straw. At least two hit straws in consecutive planes of a view module of a chamber which are compatible with the staggering of the planes form a view-hit; a pattern recognition algorithm is applied to determine the position of a view-hit in the NA62 reference frame using the measured R of the hit straws. View-hits are clustered in each straw chamber to provide space points corresponding to the passage of a particle, the number of views forming a space point being dependent on the position of the space point itself. A pattern recognition algorithm groups space points of different chambers to provide candidate tracks; this algorithm exploits the reconstruction of track segments between chambers 1 and 2, and 3 and 4, respectively and their compatibility with respect to the bending magnet in the xz plane. A fit using a recursive Kalman filter technique finally provides the measurement of the track parameters and the quality of the track; the fit takes into account the full 3-dimensional measured map of the MNP33 field and of the fringe field between chambers. The residuals of the track fit in each straw are used to correct the straw position for hardware mis-alignments with precision below 30 μm. $K^+ \to \pi^+\pi^+\pi^-$ provides further correction to the measured momentum of the track due to residual chamber mis-alignment and overall scale of the magnetic field of the bending magnet; these corrections are below per-mille and are computed by looking at the dependence of the measured K^+ mass on the π^- momentum and comparing the K^+ mass with the PDG value [3], respectively. The average of the trailing time of the straw hits forming a track gives the STRAW track time with a resolution of about 6 ns.

5.5 CHOD

CHOD reconstruction is based on coincidences of signals in the two channels associated to each of the 152 tiles. The CHOD times are defined as mean time of the two signals; "loose" candidates based on single signals are also considered. The channels are aligned

in time with respect to the KTAG, the time resolution is 1.5 ns and the detector efficiency greater than 99%.

5.6   NA48-CHOD

Scintillator slabs are aligned in time with respect to the KTAG; a time offset is derived for each crossing between slabs of corresponding quadrants of vertical and horizontal planes to account for the time propagation of the light along the scintillator; the time is also corrected for slewing. For each event a horizontal and vertical slab compatible with the passage of a charged particle are coupled to form a NA48-CHOD candidate; the time of the candidate is the average time of the two slabs and the position is the centre of the square formed by the slab intersection. The time resolution is measured in the range of 200/300 ps. The $K^+ \to \pi^+ \nu \bar{\nu}$ analysis makes use of the STRAW track as a seed to choose the slabs to be paired off; the best pair is selected minimizing a linear discriminant built with the time difference between the two slabs, the distance of the candidate from the track impact point position and the difference between the time candidate and the STRAW track time. Alternatively all the possible combination of slabs within ±10 ns and in time within 25 ns from the trigger time are considered; the candidate closest in space to the track impact point position is associated to the track at analysis level in this case.

5.7   RICH

RICH channels are aligned in time with respect to the KTAG. Two different algorithms are implemented for ring pattern recognition and reconstruction. The first one makes use of the track momentum and direction and of the NA48-CHOD time candidate matched to the track to group RICH hits associated to a track; ring and track parameters are combined to form a likelihood for each different mass hypothesis (e^+, μ^+, π^+, K^+). The second algorithm groups RICH hits in time and a ring is fitted assuming the passage of a single particle; the ring χ^2 is used as a quality criterion for reconstruction. This reconstruction allows the ring parameters to be measured independently of the STRAW track, providing a measurement of the momentum of a particle under a certain mass hypothesis independent of the one measured in the STRAW; it is clearly suited only for analysis with a single positive track in the final state, like $K^+ \to \pi^+ \nu \bar{\nu}$. Samples of e^+ are used to calibrate the RICH response. In this document rings reconstructed with the two algorithms are referred to as "track-based" and "standalone", respectively. The time resolution of a ring is measured to be about 100 ps.

5.8   LKr

The cells belonging to a single readout module (CREAM) of the LKr are aligned in time with respect to the KTAG; the time measured by the single cells is aligned further using positrons selected kinematically. Clusters are reconstructed in LKr grouping cells within 110 mm from a seed, where a seed is a cell with at least 250 MeV deposited and an energy greater than the average energy of the 3×3 surrounding cells; the energy of the cluster is the sum of the energy of the cells; the cluster time is the time of the seed; the position of the clusters is the barycentre of the cells weighted with the energy in the cells. Corrections

to cluster energy and position are applied to treat clusters close in space or in time and to handle the presence of dead cells; the energy of the clusters is corrected further to account for a non linearity induced by the online zero suppression. A MIP releases on average 550 MeV. Typical time resolutions are 500 ps for electromagnetic clusters with energy above 3 GeV and about 1 ns for hadronic and MIP clusters. Additionally, a different reconstruction algorithm is used by analyses requiring the highest LKr efficiency; in this case energy depositions of at least 40 MeV are clustered geometrically looking at adjacent cells, where two cells are defined adjacent if separated by less than 100 mm; energy, time and position of clusters are defined as above and the energy is also corrected for non linearity. Clusters from this latter reconstruction are referred to as "auxiliary clusters" in the following.

5.9   MUV1 and MUV2

The MUV1 and MUV2 clusters are reconstructed starting from the track impact position. The most energetic channel in a window of ± 150 mm around the expected impact point and within 20 ns from the track time is used as seed for the cluster reconstruction. The energy in the neighbouring channels is then summed up until two consecutive empty channels are found or the distance from the seed is greater than 7 channels (5 in the MUV2). Cluster energy is calibrated using weighting factors extracted from dedicated Geant4 simulations and tested on specific samples of pions and muons.

5.10   MUV3

MUV3 reconstruction is based on coincidences of signals in the two PMTs associated to each of the 148 tiles. The MUV3 times are defined as the later of the two channel times to avoid bias due to early Cherenkov light signals produced by muons traversing the PMT windows; "loose" candidates based on single signals are also considered. The channels are aligned in time with respect to the KTAG, the time resolution is about 500 ps and the efficiency of muon detection above 99.5%.

5.11   LAV

LAV signals are discriminated using two threshold settings. This allows a flexible reconstruction of LAV hits including time slewing corrections. A hit may be reconstructed from up to four time measurements, corresponding to the leading- and trailing-edge times on the high and low thresholds. The algorithm used to correct for slewing depends on how many and which of the edges are used to reconstruct the hit: if both leading edges are present, the slewing correction is based on the difference between the high- and low-threshold crossing times; if only the low threshold is crossed, the slewing correction is based on a fit to the measured distribution of leading-edge time as a function of the time over threshold. After the application of slewing corrections, time resolutions at the level of 1 ns are achieved for all LAV stations.
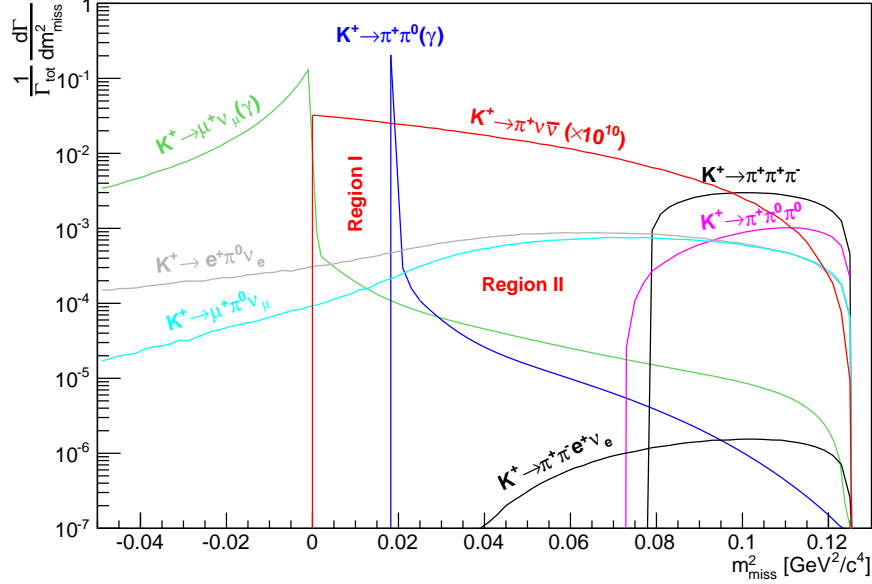
Figure 3: Theoretical m_{miss}^2 distribution for signal and backgrounds of the main K^+ decay modes: the backgrounds are normalized according to their branching ratio; the signal is multiplied by a factor 10^{10}.

5.12 IRC and SAC

Both TDC and FADC FE electronic (CREAM) are used to readout IRC and SAC. The hits from TDC are reconstructed as for LAV. The time is aligned to the KTAG, corrected for slewing and the resolution is measured to be better than 1 ns. Signals from CREAM modules are fitted with a parabola to get a measurement of the time and the amplitude. After baseline subtraction, the relation between pulse amplitude and energy release is determined channel by channel using a sample of $K^+ \rightarrow \pi^+\pi^0$. The energy resolution of the detectors for photons at 5 GeV is better than 12% in the SAC and around 30% for IRC. The time is aligned to the KTAG and the resolution is measured to be better than 1.5 ns.

5.13 MUV0 and HASC

Signals from the TDC FE module of MUV0 are treated as in LAV to reconstruct hits. Each signal from the SiPMs of HASC is digitized using a discriminator with 4 different ADC thresholds and is reconstructed including T0s and slewing corrections.

6 Data Analysis

The physics analysis presently on-going are organized in three analysis working groups (WG):

- $\pi\nu\nu$ Analysis WG;

- Exotics Physics Searches Analysis WG;

- Rare and Forbidden Decays Analysis WG.

In addition a Data Quality and a Software WG take care of detector reconstructions together with individual sub-detector WGs, data preparation, quality, processing and Monte Carlo (MC) production.

The status of the data analysis is reported in the following sections.

7 $K^+ \to \pi^+ \nu \bar{\nu}$ Analysis

The $K^+ \to \pi^+ \nu \bar{\nu}$ analysis (referred to as "$\pi \nu \nu$ analysis" in the following) is carried out on data from sample A only because it needs the GTK fully working and no downscaling to the trigger. The number of kaon decays collected would allow one Standard Model (SM) $K^+ \to \pi^+ \nu \bar{\nu}$ event to be observed, for a signal acceptance in the percent range (SM predicts the branching ratio to be 8.4×10^{-11} [4]). The goal of the analysis on 2016 data is to study the single event sensitivity of the apparatus down to 1 event over 10^{10}. A preliminary exploratory analysis has been performed on about 2.3×10^{10} K^+ decays in 60 m fiducial region from sample A (5% of the 2016 total statistics).

The signature of the signal is one track in the initial and final state. The main kinematic variable is $m_{miss}^2 \equiv (P_K - P_{\pi^+})^2$, where P_K and P_{π^+} are the 4-momenta of K^+ and of the charged decay product under the π^+ mass hypothesis, respectively. Figure 3 shows the m_{miss}^2 theoretical spectrum of most of the K^+ decay modes compared to $K^+ \to \pi^+ \nu \bar{\nu}$. The analysis plans to look for signals in two regions: region 1 between $K^+ \to \mu^+ \nu$ and $K^+ \to \pi^+ \pi^0$ and region 2 between $K^+ \to \pi^+ \pi^0$ and $K^+ \to \pi^+ \pi^+ \pi^-$. Backgrounds from kaon decays entering in these regions are: $K^+ \to \pi^+ \pi^0$ and $K^+ \to \mu^+ \nu$, through non gaussian resolution and radiative tails; $K^+ \to \pi^+ \pi^+ \pi^-$ through non gaussian resolution tails; decays with neutrinos in final state. Particle identification and photon rejection complement the kinematics in background suppression. Backgrounds induced by upstream decays and beam-detector interactions are discussed later. The analysis is done with p_{π^+} between 15 and 35 GeV/c, to leave at least 40 GeV of missing energy.

The analysis proceeds through: $\pi \nu \nu$ selection; evaluation of the expected number of $K^+ \to \pi^+ \nu \bar{\nu}$ events; determination of the expected background.

The $\pi \nu \nu$ selection consists of: selection of events with a single charged particle in final state; K^+ selection and definition of the decay region; π^+ identification; veto of extra activity in time with π^+ and K^+.

7.1 Single Track Selection

An event is defined as a set of data collected in each sub-detector within a given (detector-dependent) readout window opened around the time of a trigger condition. An event must have at least one track of good quality reconstructed in STRAW consistent with a particle of positive charge. Each track must also satisfy the following requirements:

- a track should not form a decay vertex with other tracks (a decay vertex is an intersection between two or more tracks, in the region between the last GTK station and the first straw chamber, with CDA lower than 15 mm);

- the track extrapolated to the various sub-detectors must be within the geometrical acceptance of the sub-detectors themselves;
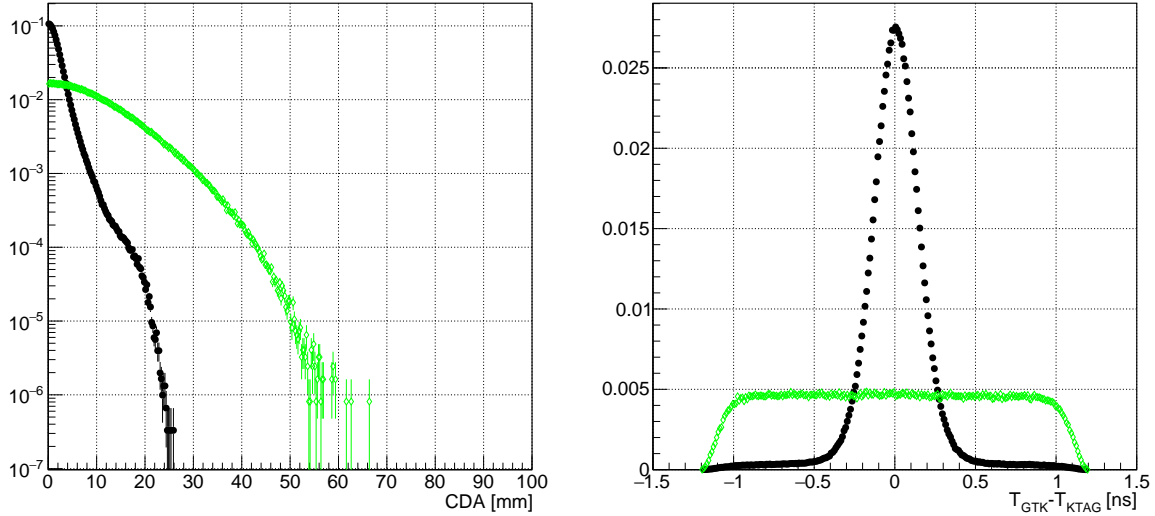
Figure 4: Left: CDA distribution of the vertex formed by a good K^+ and a π^+ track selected from $K^+ \to \pi^+\pi^+\pi^-$ events (black dots); Right: distribution of the time difference between GTK and KTAG time candidates for K^+ and π^+ selected from $K^+ \to \pi^+\pi^+\pi^-$ events (black dots); green dots are the same quantities computed with a random beam track instead of K^+ track.

- the track has to match a NA48-CHOD candidate; the time of this candidate is referred to as "pion time" in the following;

- the track has to match at least a candidate in CHOD; the CHOD candidate must be within ± 5 ns from the pion time;

- a cluster in LKr must be closer than 150 mm to the track impact point and within ± 8 ns from the pion time;

- both a track-based and a standalone ring matched to the track must be reconstructed; a standalone ring matches the track if: $\chi^2/ndf < 3$; the track slopes computed from the ring centre and measured by STRAW are compatible within 400 μrad, where the resolution of the slopes measured with the RICH is below 200 μm; the ring is within ± 3 ns from the pion time;

- MUV1 and MUV2 clusters associated if any;

- the pion time must be within ± 25 ns from the trigger time.

The track reconstructed in STRAW satisfying the above condition is called "straw track" in the following.

7.2 K^+ Selection

At least a kaon candidate must be selected in KTAG, within ± 2 ns from the pion time; the time of the kaon candidate closest to the pion time is referred to as "kaon time" in the following. The kaon time is used as a seed for GTK reconstruction. Each of the
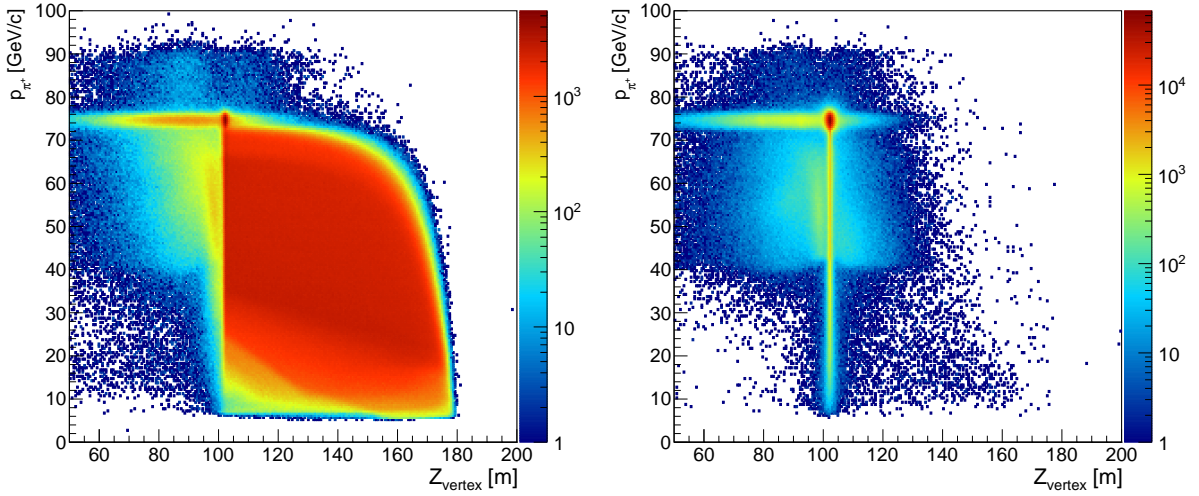
Figure 5: Distribution of π^+ momentum as a function of the z coordinate of the vertex for kaon events (left) and non kaon events (right); kaon and non kaon events are defined in the text.

GTK tracks within ± 600 ps from the kaon time are coupled to a straw track to build a vertex. The CDA of the vertex and the time difference, ΔT, of the kaon and GTK time are combined to choose the GTK track matching the straw track, referred to as "kaon track" in the following. The track choice is based on a discriminant built from functions fitted to the profile of template CDA and ΔT distributions of K^+ and random beam tracks selected on $K^+ \rightarrow \pi^+\pi^+\pi^-$ events (see Figure 4). Random beam tracks are reconstructed in GTK from hits in a time window 10 ns large and 15 ns off the kaon time. Resolution (1 σ) of CDA and ΔT are 1.5 mm and 130 ps, respectively. The GTK-Straw mis-matching probability is measured on an independent sample of $K^+ \rightarrow \pi^+\pi^+\pi^-$ selected on data taken at 40% of nominal intensity and is found to be 1.7% if the real kaon track is reconstructed; events without the real kaon track reconstructed account for another 2.5% of mis-matching probability. The reconstruction efficiency of a kaon track is 75%.

If more than one straw track is found in an event, only the track is considered whose associated candidates in KTAG, GTK, NA48-CHOD, LKr, RICH, MUV1 and MUV2 (if any) are simultaneously the closest ones to the trigger time. Such a track is referred to as "pion track" in the following. Should no track satisfy the above condition, the event is rejected. An event with a kaon track and a pion track is called "kaon event".

Events without a kaon candidate in KTAG are selected as well for control studies. In this case the same procedure described above applies to choose a GTK track matching the straw track, but the pion time is used instead of the kaon time. The matched GTK track is called "beam track" and the event is referred to as "non kaon event".

7.3 Definition of the Decay Region

The pion track momentum as a function of the longitudinal position of the vertex, Z_{vertex}, for kaon events (non kaon events) selected on control data is shown in Figure 5 left (right).
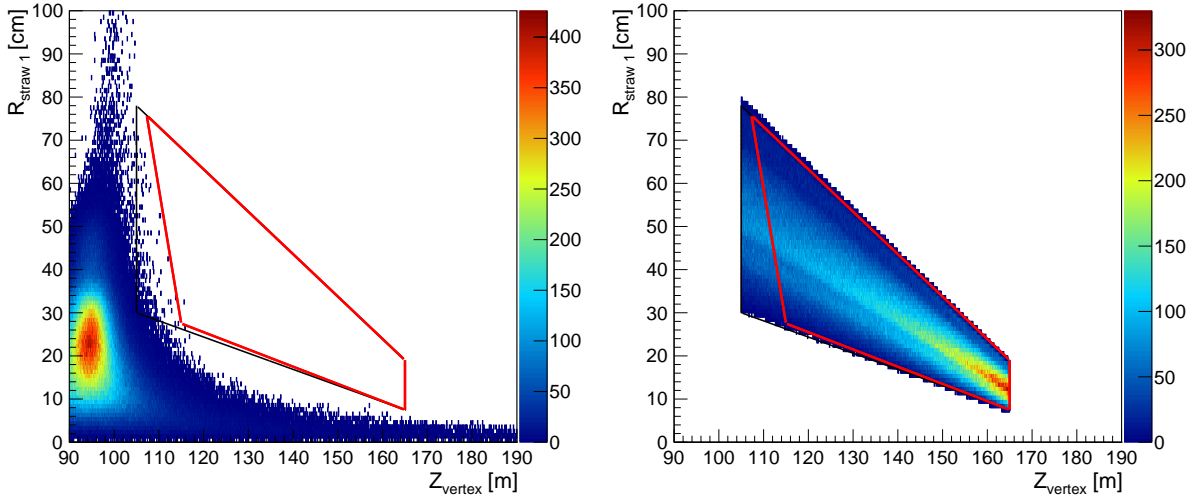
Figure 6: MC distribution of the distance of the π^+ track from the beam at first STRAW chamber as a function of the z coordinate of the vertex formed by the π^+ with a matched track in GTK, for K^+ early decays (left) and signal event (right) both with $15 < p_{\pi^+} < 35$ GeV/c. Events outside the red lines are rejected by the cuts on R_{Straw1} versus Z_{vertex} applied in the $\pi\nu\nu$ selection and described in the text. The black line following the expected profile of $\pi\nu\nu$ events is also drawn.

Besides the K^+ decays downstream of the last GTK station, also interactions of K^+ in the last GTK station and K^+ decaying upstream are sources of pion tracks. The fiducial volume is defined by $105 < Z_{vertex} < 165$ m, i.e. a 60 m long region starting 2.5 m downstream the last GTK station [5].

Early K^+ decays should not have a kaon track in GTK; therefore they can be a source of background to $K^+ \to \pi^+ \nu\bar{\nu}$ only in case of GTK-Straw mis-matching and, consequently, wrong vertex reconstruction. MC simulations show that early decays with a pion detected downstream may happen in the last two dipole magnets of the second achromat. In this case the vertex can be mistaken up to several tens of metres, mainly because of the large transverse beam size. The rejection of this background relies primarily on the decay vertex and particle identification, since any additional energy from the decay is likely to be absorbed by the material of the beam elements. However the final collimator puts constraints on the kinematics of the accepted early decays. As a result the distance of the pion track impact point at the first STRAW chamber from the nominal beam position, R_{Straw1}, as a function of Z_{vertex} is distributed differently for early decays and signal events (Figure 6). A cut in the (R_{Straw1}, Z_{vertex}) plane is therefore applied to suppress early decays. As a consequence the starting point of the fiducial volume is moved by 5-10 m downstream to the proposed 105 m, corresponding to 10% loss of signal acceptance for K^+ decaying in the decay volume.

Kaon inelastic interactions in the last GTK station are a source of background if the additional energy goes undetected and either a prompt pion track is emitted and the vertex is wrongly reconstructed, or a long-lived particle (K_S or K^+) is produced almost parallel to the original K^+ and subsequently decays. The above cut against early decay suppresses also inelastic interactions. Additional cuts are:

- no hits in CHANTI within ± 3 ns from the pion time, a hit being a coincidence of x and y counters; the signal loss induced by the accidental activity in CHANTI is measured using $K^+ \to \mu^+ \nu$ and is found to be around 1% at 40% of nominal intensity;

- time over threshold of GTK hits below 24 ns;

- no hit in the last GTK station within 20 mm from the pion track extrapolated back to the GTK station itself;

- the pion track extrapolated back to the end of the final collimator is outside the aperture of the collimator.

The efficiency to detect pion interactions in the last GTK station with CHANTI is measured using non kaon events. Pions originating at the last GTK station and with momentum between 15 and 35 GeV/c are selected using particle identification criteria in calorimeters and RICH described in Sections 7.6 and 7.7. The efficiency is found to be 85%; the inefficiency is dominated by the acceptance for additional charged tracks produced in the interaction.

7.4 Definition of Signal and Background Regions

Figure 7 shows the distribution of the reconstructed m_{miss}^2 as a function of the momentum of the pion track for kaon events selected with the control trigger; the π^+ mass is assigned to the pion track. $K^+ \to \pi^+\pi^0$, $K^+ \to \mu^+\nu$ and $K^+ \to \pi^+\pi^+\pi^-$ decays are clearly visible. Alternatively the m_{miss}^2 can be reconstructed using either the nominal kaon 3-momentum instead of the GTK measurement, $m_{miss}^2(No\ GTK)$, or the pion track momentum measured by the RICH instead of STRAW assuming the π^+ mass, $m_{miss}^2(RICH)$. Although $m_{miss}^2(No\ GTK)$ and $m_{miss}^2(RICH)$ have about 3 times worse resolution than m_{miss}^2, they provide a way to control non gaussian tails because they are not sensitive to kaon track 3-momentum mis-measurements in GTK and pion track momentum mis-measurement in STRAW, respectively. Two three-dimensional signal regions are defined by the following conditions applied on m_{miss}^2, $m_{miss}^2(No\ GTK)$ and $m_{miss}^2(RICH)$

- **Region 1**: $(0, 0.01)$ GeV$^2/c^4$;

- **Region 2**: $(0.026, 0.068)$ GeV$^2/c^4$.

Similarly three background regions are defined:

- **$\pi^+\pi^0$ region**: $|m_{miss}^2 - m_{\pi^0}^2| < 3 \cdot \sigma(m_{miss}^2)$ and $0.01 < m_{miss}^2(RICH) < 0.03$ GeV$^2/c^4$;

- **$\mu^+\nu$ region**: $-0.04 < m_{miss}^2 < m_{miss}^2(\mu\nu, max) + 3 \cdot \sigma(m_{miss}^2)$ GeV$^2/c^4$, where $m_{miss}^2(\mu\nu, max)$ is $(m_{\pi^+}^2 - m_{\mu^+}^2) \cdot (1 - 75/35)$;

- **$\pi\pi\pi$ region**: $m_{miss}^2 > 4 \cdot m_{\pi^+}^2 - 3 \cdot \sigma(m_{miss}^2)$.

where $\sigma(m_{miss}^2)$ is the resolution of m_{miss}^2.

The requirement

- $15 < p_{\pi^+} < 35$ GeV/c,

completes the definition of both the signal and the background regions.
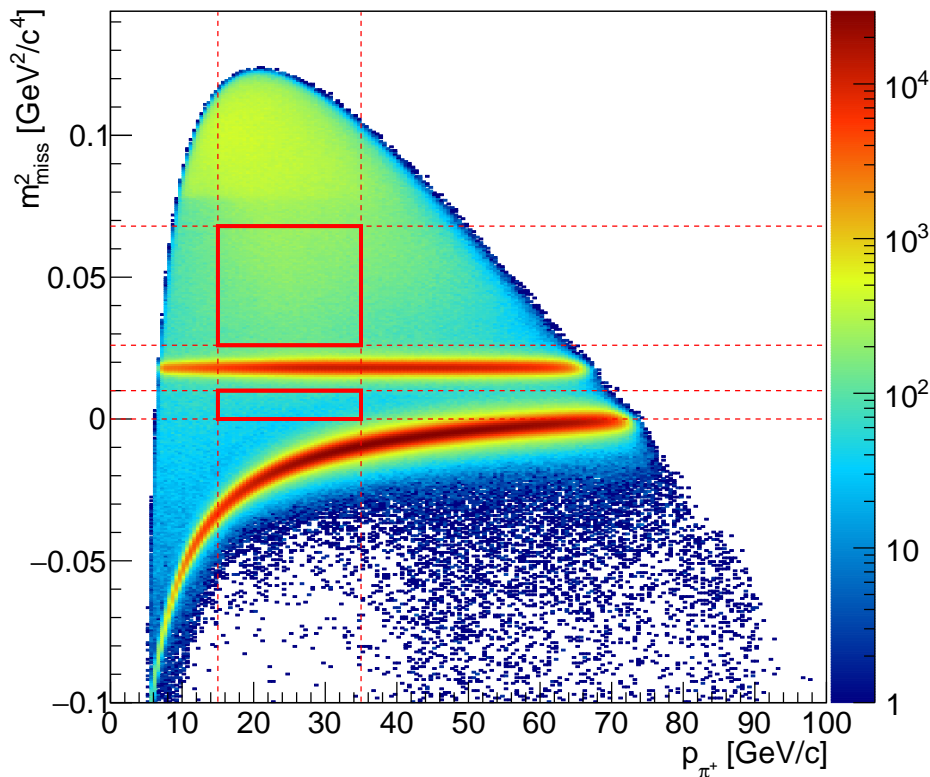
Figure 7: Distribution of m^2_{miss} as a function of pion momentum for kaon events selected on control data. The signal regions (red box) in the (m^2_{miss}, p_{π^+}) plane are drawn for reference.

7.5 Kinematic Reconstruction Performances

The fraction of $K^+ \to \pi^+\pi^0$ and $K^+ \to \mu^+\nu$ events entering in the signal regions is measured using corresponding samples of K^+ decays collected by the control trigger concurrently with the PNN trigger. Both selections start from kaon events. Two electromagnetic-like clusters in LKr are looked for to select $K^+ \to \pi^+\pi^0$; the K^+ decay vertex is computed assuming that the clusters originated from γs' from π^0 decay and is required to be within $115 < Z_{vertex} < 165$ m. The π^0 selection is kept fully independent of K^+ and π^+ kinematical variables to avoid any bias in the reconstructed m^2_{miss}. The same criteria for particle identification ("particle ID") and photon rejection in LAV, IRC and SAC used to select $K^+ \to \pi^+\nu\bar{\nu}$ (see Sections 7.6, 7.8) are applied also to select $K^+ \to \pi^+\pi^0$; a cut on the extra activity in LKr cleans the sample further. $K^+ \to \mu^+\nu$ are selected requiring a hit in MUV3 associated to the track within ± 5 ns from the pion time and MIP clusters in LKr, MUV1 and MUV2. No RICH particle ID requirement is applied to the muon to avoid biasing in the kinematics. The range $115 < Z_{vertex} < 165$ m is considered in the selection of this sample. Photon rejection is applied like in $K^+ \to \pi^+\nu\bar{\nu}$ selection (Section 7.8).

The top-row plots in Figure 8 show the distribution of $K^+ \to \pi^+\pi^0$ control events with $15 < p_{\pi^+} < 35$ GeV/c in the $(m^2_{miss}(No\,GTK), m^2_{miss})$ and $(m^2_{miss}(RICH), m^2_{miss})$
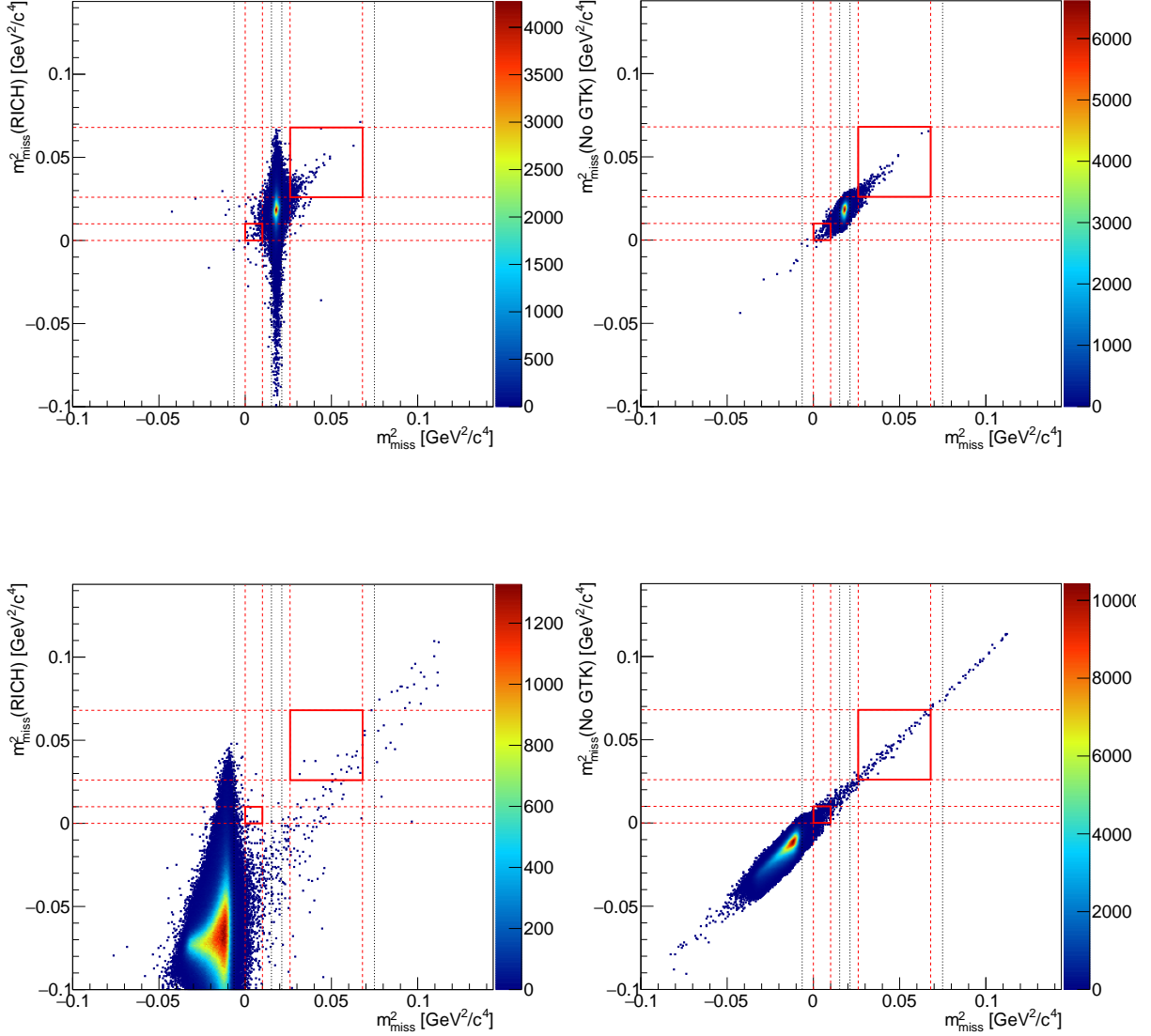
Figure 8: Top-row: distribution of $m^2_{miss}(RICH)$ vs m^2_{miss} (left) and $m^2_{miss}(No\ GTK)$ vs m^2_{miss} (right) for $K^+ \to \pi^+\pi^0$ events selected for kinematic studies. Bottom-row: same distribution for $K^+ \to \mu^+\nu$. The red tick boxes correspond to the two-dimensional projections of the signal region; the light dashed black line to the kinematical limiting defining $K^+ \to \mu^+\nu$, $K^+ \to \pi^+\pi^0$ and $K^+ \to \pi^+\pi^+\pi^-$ regions.
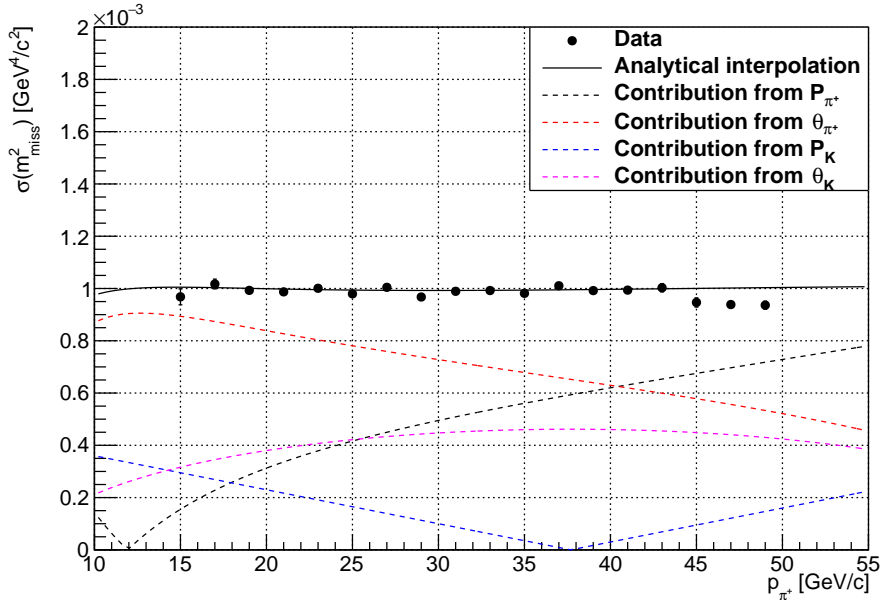
Figure 9: Gaussian resolution of the m_{miss}^2 measured on a $K^+ \to \pi^+\pi^0$ sample, as a function of pion momentum. The black solid line is an analytical interpolation using the expected resolutions for GTK and STRAW. The dashed lines correspond to the contributions of the individual quantities entering in the computation of m_{miss}^2.

planes. The fraction of $K^+ \to \pi^+\pi^0$ in the signal regions (region 1 and 2) is estimated to be $(5.9 \pm 0.2) \times 10^{-4}$ (1.6×10^{-4} and 4.2×10^{-4}). Variations of $\pm 0.4 \times 10^{-4}$ are observed among runs, not clearly correlated with the intensity. A two times larger fraction of events is measured if signal regions are defined by cuts on m_{miss}^2 only. A similar measurement is performed on $K^+ \to \mu^+\nu$ (bottom-row plots in Figure 8). In this case only the fraction of events entering the signal regions projected onto the $(m_{miss}^2(No\ GTK),\ m_{miss}^2)$ plane is considered, because the rejection factor induced by $m_{miss}^2(RICH)$ is fully correlated with the RICH particle ID. The fraction of $K^+ \to \mu^+\nu$ in this region is $(2.9 \pm 0.1) \times 10^{-4}$ (2.5×10^{-4} and 0.4×10^{-4}). A $\pm 0.3 \times 10^{-4}$ variation is observed among runs, linearly dependent on the beam intensity, ranging from 5% to 50% of the nominal one. The above results are a factor 3 larger than previous MC estimations [6]. The fraction of $K^+ \to \pi^+\pi^+\pi^-$ events entering the signal regions is 10^{-4} from MC simulations. A measurement on data of the $K^+ \to \pi^+\pi^+\pi^-$ kinematic rejection factor is in progress.

The resolution of the m_{miss}^2 is measured on the $K^+ \to \pi^+\pi^0$ sample. Two gaussian functions are fitted to the m_{miss}^2; the second gaussian accounts for the worsening of the resolution due to events with mis-matched K^+. Figure 9 shows the result of the fit as a function of the π^+ momentum. The resolution is fully compatible with the designed resolutions of GTK and STRAW and is about $\sigma(m_{miss}^2) = 10^{-3}$ GeV^2/c^4.

7.6   Particle ID with Calorimeters

Events are rejected if a pion track has a MUV3 candidate matched in space within ± 5 ns from the pion time or clusters matched in LKr, MUV1 and MUV2 compatible with a MIP. The energy associated to the pion track in LKr, MUV1 and MUV2 is exploited to separate
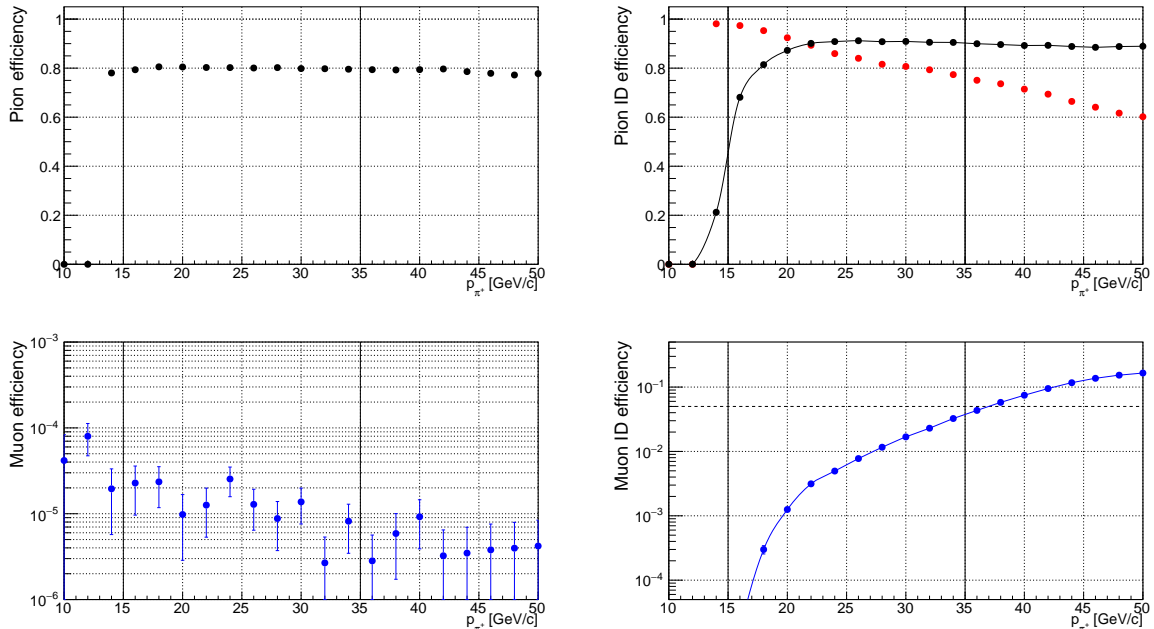
Figure 10: Left column: efficiency of pion (top) and muon (bottom) identification after requiring pion identification with calorimeters and MUV3. Right column: efficiency of standalone ring reconstruction (top black dots), pion (top red dots) and muon (bottom) identification after applying the π^+ ID condition described in the text on the reconstructed mass from standalone ring.

μ^+ and π^+ further. A discriminant to separate pions, muons and positrons is built using a Boosted Decision Tree technique with 13 input variables describing the energy measured in the calorimeters with respect to the track momentum, the sharing of the energy between calorimeters, the shape of the showers and the track−cluster matching distances. The tree is trained on samples of π^+, μ^+ and e^+ taken from $K^+ \to \pi^+\pi^0$, $K^+ \to \mu^+\nu$ and $K^+ \to \pi^0 e^+\nu$ selected using kinematics, RICH and π^0. These samples cover the kinematic regions of interest of the particles from signal and background. A cut on the discriminant is applied in the $\pi\nu\nu$ analysis to identify π^+s. Events with a π^+ releasing more than 80% of its energy in LKr are rejected to suppress e^+ further.

Samples of π^+ and μ^+ selected on different set of data taken with control trigger are used to assess the performances of the particle separation. The selection of these samples closely follows the $\pi\nu\nu$ selection as described in Section 7.5. The main differences are the particle ID with calorimeter not applied and kinematic cuts added to suppress backgrounds. The left column of Figure 10 shows the efficiency of pion identification and the residual fraction of muons as a function of p_{π^+}.

7.7   Particle ID with RICH

Particle identification with RICH requires: track-based ring with maximum likelihood under the π^+ hypothesis; particle mass measured with the standalone ring and STRAW momentum between 0.133 and 0.2 GeV/c^2; kinematic cuts applied to select the signal region projected onto the $(m^2_{miss}(RICH), m^2_{miss})$ plane, as described in Section 7.5.

As in the case of calorimeters, particle ID performances with RICH are studied on
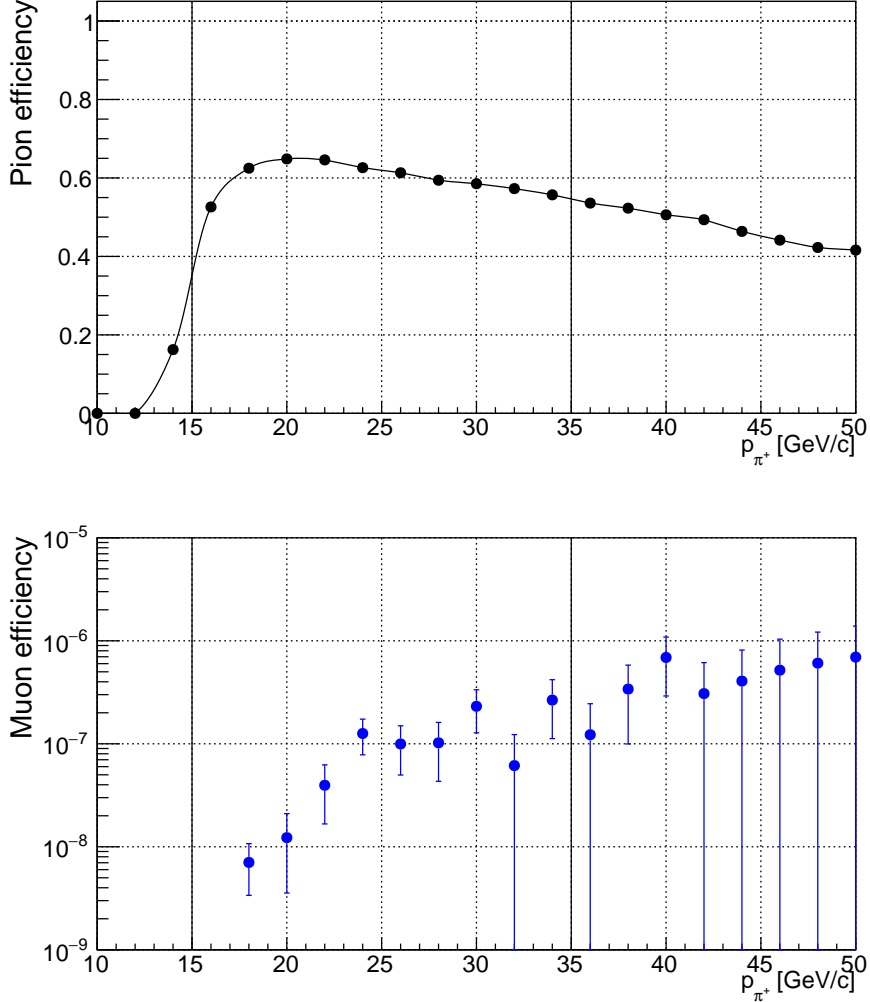
Figure 11: Combined pion (top) and muon efficiency (bottom) after pion identification in calorimeter and RICH, assuming that the two detectors are independent.

samples of π^+ and μ^+. Their selection is similar to the one described in Section 7.6, with the difference that calorimeters are used for particle ID instead of the RICH. The right column of Figure 10 shows the efficiency of standalone ring reconstruction, the pion identification efficiency and the residual fraction of muons using the above cuts on particle mass.

The final π^+, μ^+ separation performances are summarised in Figure 11. The particle ID from RICH and calorimeter are assumed to be independent and only the RICH mass cut from the standalone ring is included.

7.8 Photon Rejection

The following conditions are applied to veto events with photons:

- clusters and auxiliary clusters in LKr must be at least 150 mm distant from the pion track extrapolation; clusters with energy greater than 2 GeV must be within
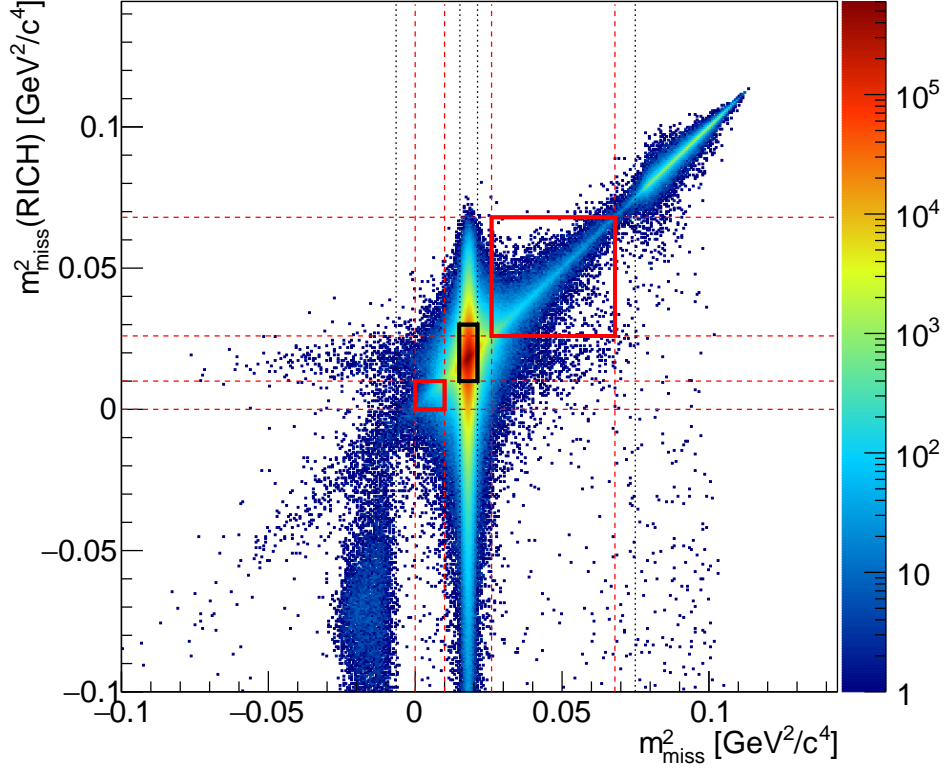
Figure 12: Distribution in the $(m^2_{miss}(RICH), m^2_{miss})$ plane of events triggered by the PNN trigger line and passing the $\pi\nu\nu$ selection before the photon rejection and with $15 < p_{\pi^+} < 35$ GeV/c. The signal regions (red tick box) and the $\pi\pi$ region (black tick box) are drawn.

$(-10, +15)$ ns from the pion; clusters with energy lower than 2 GeV within $(-5, 8)$ ns; auxiliary clusters with energy greater than 1 GeV within ± 8 ns;

- at least one block in LAV hit, the signal satisfies specific quality criteria and is within ± 5 ns from the pion time;

- a signal in IRC must have at least a TDC measurement of the leading time passing the low threshold and must be within ± 5 ns from the pion time; otherwise the energy measured by the CREAM must be greater than 1 GeV and the signal must be within ± 5 ns from the pion time;

- any signal in SAC measured by the TDC within ± 5 ns from the pion time is considered; otherwise a signal in SAC measured by the CREAM should be present, satisfying the same conditions as for the IRC.

The fraction of $K^+ \to \pi^+\pi^0$ events passing the photon conditions is measured as:

$$\epsilon_{\pi^0} = \frac{n^{PNN}_{\pi\pi}}{D^{control} \cdot N^{control}_{\pi\pi}}; \tag{1}$$

23
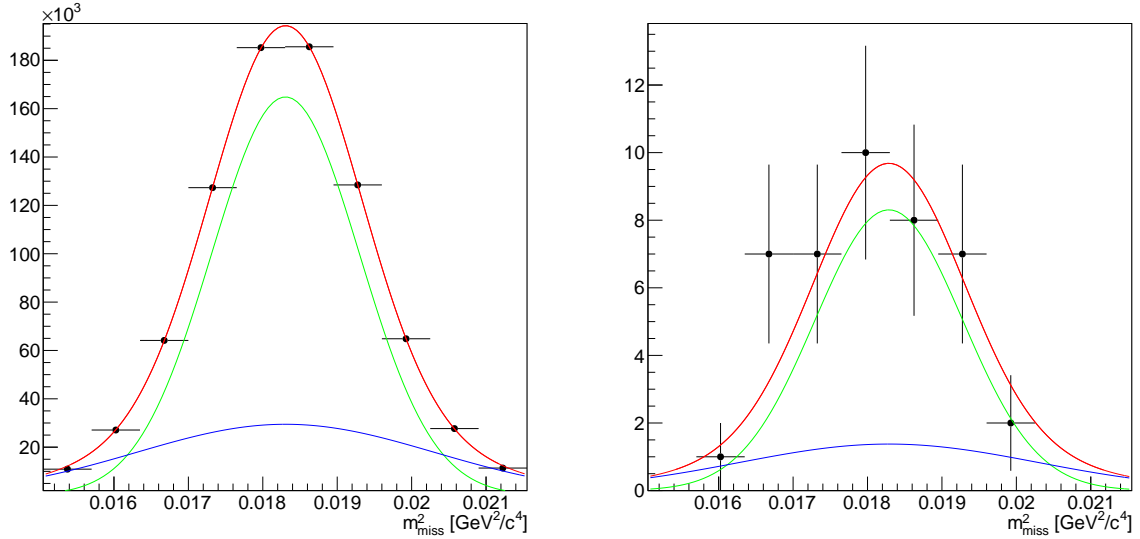
Figure 13: Distribution of events in the $\pi\pi$ region before (left) and after (right) photon rejection. Events before photon rejection are from control trigger and must be multiplied by the downscaling factor (400) to get the total number of $K^+ \to \pi^+\pi^0$ before photon rejection. The 2-gaussian fit is superimposed. The overall scale is the only free parameter in the fit of the events after photon rejection, the other parameters are fixed to the value obtained by the fit before photon rejection.

here $n_{\pi\pi}^{PNN}$ is the number of $K^+ \to \pi^+\pi^0$ passing the $\pi\nu\nu$ selection on PNN triggered data and also the photon veto conditions; $N_{\pi\pi}^{control}$ is the number of $K^+ \to \pi^+\pi^0$ passing the $\pi\nu\nu$ selection on control data without applying the photon veto conditions; $D^{control}$ is the downscaling factor of the control trigger (400 for data from sample A). $K^+ \to \pi^+\pi^0$ events are counted in the $\pi^+\pi^0$ region defined in Section 7.4 (Figure 12).

Two gaussian functions fit the m_{miss}^2 peak of events in the $\pi^+\pi^0$ region before photon rejection, as described in Section 7.5 (Figure 13 left). The same functions are used to fit the m_{miss}^2 peak of events in the $\pi^+\pi^0$-region after photon rejection (Figure 13 right); in this case the only free parameter of the fit is the overall normalization, with the means, standard deviations and relative ratio of the two gaussian functions kept fixed to the values obtained by the fit before photon rejection. $N_{\pi\pi}^{control}$ and $n_{\pi\pi}^{PNN}$ are the integral of the fitted functions. The statistics analysed so far translates to about 3.3×10^8 $K^+ \to \pi^+\pi^0$ events selected before photon rejection and 41 after, corresponding to

$$\epsilon_{\pi^0} = (1.2 \pm 0.2) \times 10^{-7}. \tag{2}$$

The effect of a possible e^+ background in the $\pi^+\pi^0$-region is evaluated by varying the cuts on $m_{miss}^2(RICH)$ within ± 0.004 GeV^2/c^4 and is found to be $\pm 0.1 \times 10^{-7}$.

A sample of $K^+ \to \mu^+\nu$, selected with kinematics and particle ID only, is used to evaluate the signal loss induced by accidental activity in photon detectors. It is found to be 16% at 40% nominal intensity, increasing almost linearly from 7% to 18% for a beam intensity varying from 5% to 50% of the nominal one. Signal losses from LAV alone are 11% at 40% of nominal intensity, 5% from LKr, 2.5% from IRC and SAC, partially correlated between detectors. Signal losses from π^+ interactions in the material in front of LKr are studied using 75 GeV/c beam π^+ elastically scattered off the last GTK station.

24

These tracks are selected among non kaon events originating from Z_{vertex} at the position of the last GTK station (Figure 5) and identified as π^+ (Section 7.6). A 2% contribution is measured in addition to the accidental losses quoted with $K^+ \to \mu^+\nu$. The enhancement is due to a stronger veto from LKr (+2%) and IRC/SAC (+0.5%). Preliminary studies show that accidental losses can be reduced after optimization of the photon rejection criteria, especially in LAV.

7.9 Multi Charged Particle Rejection

The $\pi\pi\pi$ region defined in Section 7.4 is used as a benchmark to study the suppression of K^+ decays with more than one charged particle in the final state (referred to as "multi-charged events"). MC simulations and observation of data in the $\pi\pi\pi$ region show that among the $\pi\nu\nu$ selection criteria previously described those contributing to the reduction of multi-charged events are:

- L0 trigger conditions on CHOD multiplicity (Section 3.1);

- requirement for a STRAW track not to form a vertex with other tracks (Section 7.1);

- criteria described in Section 7.2 to define a pion track;

- cut in the (R_{Straw1}, Z_{vertex}) plane described in Section 7.3;

- veto of the activity in the last LAV station and IRC (Section 7.8);

- kinematic cuts to define the signal region (Section 7.5).

In addition specific variables are considered to suppress further multi-charged events (referred to as "multi-charged variables"):

- for each hit in straw chamber 2 (4) not belonging to any tracks, segments are reconstructed in the non bending plane yz together with the decay vertex position; hits in chambers 1 (3) not belonging to any tracks are classified according to the significance $d/\sigma(d)$ of their distance d from any segment, where $\sigma(d)$ is the expected resolution of d; the minimum significance S_d for each event is then obtained;

- assuming a single π^+ in the final state, a probability is assigned to each event computed from the expected and detected number of hits in RICH in time with the pion;

- number of hits in CHOD in time with the pion, not associated to the pion track, but matching in time and space either hits in NA48-CHOD or cells in LKr or clusters in MUV1;

- any HASC and MUV0 hit in time with the pion.

The multi-charged variables provide an additional $K^+ \to \pi^+\pi^+\pi^-$ suppression factor ranging from 10 to 50, depending on how they are combined in the analysis. Signal losses are evaluated using $K^+ \to \mu^+\nu$ events and are below 10% at 40% of nominal intensity, with 5% coming from the condition on track segments alone. Optimization of the multi-charged selection is under study, showing sizable margins for improvements.

A set of cuts on the multi-charged variables providing an additional $K^+ \to \pi^+\pi^+\pi^-$ reduction factor of 10 and 10% signal losses is considered in the results presented below.

7.10 Trigger efficiency

$K^+ \to \pi^+\pi^0$ and $K^+ \to \mu^+\nu$ events selected on control trigger data are used to measure the efficiency of each of the conditions forming the L0 PNN trigger. To this extent the trigger logic is replicated at offline level and events are counted before and after a specific trigger condition. The measured efficiencies are: 0.96 for RICH, 0.985 for LAV veto, 0.95 for CHOD multiplicity veto conditions, and 0.94 for MUV3 veto. The signal efficiency of the LKr L0 trigger is measured using $K^+ \to \pi^+\pi^0$ events with the two γs outside the LKr acceptance and is found to be about 0.90.

The L1 trigger efficiency is measured using a fraction of L0 triggers, called AutoPass (AP) saved directly on tape without being cut by L1. L1 trigger performances are expressed in terms of "signal efficiency" and "data reduction factor". The former denotes the number of L1 triggered events with respect to a considered input, the latter is computed as the ratio of the L0 triggers in input over the L1 triggered events. For L1 PNN trigger, a control sample of $K^+ \to \pi^+\pi^0$ decays with both photons reconstructed in the LKr and $15 < p_{\pi^+} < 35$ GeV/c is considered. A preliminary measurement at 40% of nominal intensity indicates 93% signal efficiency for a data reduction factor of 17.

7.11 Signal Evaluation

A simple counting method is applied to assess the sensitivity of the analysis. $K^+ \to \pi^+\pi^0$ events passing the $\pi\nu\nu$ selection on control triggered data, without applying photon and multi-charged rejection, are used for normalization. The number of expected signal events $N_{\pi\nu\nu}^{exp}$ is computed as:

$$N_{\pi\nu\nu}^{exp} = D^{control} \cdot N_{\pi\pi}^{control} \cdot \frac{BR_{\pi\nu\nu}}{BR_{\pi\pi}} \cdot \frac{A_{\pi\nu\nu}}{A_{\pi\pi}} \cdot \epsilon^{trig}; \tag{3}$$

here $BR_{\pi\nu\nu}$ and $BR_{\pi\pi}$ are the branching ratios of the $K^+ \to \pi^+\nu\bar{\nu}$ and $K^+ \to \pi^+\pi^0$ decays, respectively; $A_{\pi\nu\nu}$ and $A_{\pi\pi}$ their acceptances; ϵ^{trig} the PNN trigger efficiency for signal events uncorrelated with the selection efficiency. The signal acceptance is factorised as:

$$A_{\pi\nu\nu} = A_{sel} \cdot A_{kine} \cdot (1 - \eta_{\gamma-loss}) \cdot (1 - \eta_{mult}); \tag{4}$$

here the acceptance A_{sel} after the selection in common between signal and normalization and the acceptance A_{kine} after applying the kinematic cuts to define the signal and background region (Section 7.5) are assumed to be independent; A_{sel} includes the effect of geometrical cuts, GTK - straw track association, definition of the decay region, π^+ ID both in calorimeters and RICH, segment rejection and pion momentum cut between 15 and 35 GeV/c; $\eta_{\gamma-loss}$ and η_{mult} are the fractions of signal rejected by the photon and multi-charged veto criteria, respectively. η_{mult} does not contain the effect of the segments condition because it is applied in the selection of both normalization and signal.

The normalization channel acceptance can be written as:

$$A_{\pi\pi} = A_{sel} \cdot A_{kine}, \tag{5}$$

where A_{kine} is the acceptance after the cuts defining the $\pi^+\pi^0$ region.

To make a first evaluation of the expected number of signal events, A_{sel} is assumed equal for $K^+ \to \pi^+\nu\bar{\nu}$ and $K^+ \to \pi^+\pi^0$. MC simulations suggest $A_{kine} = 0.6$ for $K^+ \to$

$\pi^+\nu\bar{\nu}$ and 0.86 for $K^+ \rightarrow \pi^+\pi^0$ events. The measurement of the trigger efficiency is described in Section 7.10. However the trigger efficiency is highly correlated with the selection efficiency because most of the trigger conditions are also applied at analysis level. The difference of timing windows and variable resolutions between online and offline accounts for the uncorrelated part of the trigger efficiency. A measurement of the uncorrelated trigger efficiency is on-going. Preliminary studies show that a conservative estimate of ϵ^{trig} is 0.85. This value is applied to all the data analysed, independently of track momentum. $\eta_{\gamma-loss}$ and η_{mult} are measured run by run as described in Section 7.8 and 7.9. Finally the SM prediction is taken for $BR_{\pi\nu\nu}$ and the PDG value for $BR_{\pi\pi}$.

The result from 5% of the 2016 data analyzed so far is:

$$N^{exp}_{\pi\nu\nu} = 0.064. \tag{6}$$

Because the data analysed corresponds to about 2.3×10^{10} kaon decays, $N^{exp}_{\pi\nu\nu}$ translates into a signal acceptance of about 0.033.

A more precise evaluation of the acceptances and trigger efficiency is on-going, as well as the use of other K^+ channels for normalization. A momentum and intensity dependent analysis is also planned.

7.12   Background Evaluation

Expected backgrounds from $K^+ \rightarrow \pi^+\pi^0$, $K^+ \rightarrow \mu^+\nu$ and $K^+ \rightarrow \pi^+\pi^+\pi^-$ are evaluated on data, counting the number of events passing the $\pi\nu\nu$ selection in $\pi^+\pi^0$, $\mu^+\nu$ and $\pi\pi\pi$ regions, respectively. The events are then multiplied by the kinematic factors described in Section 7.5. The rejection factor for region 1(2) is applied to $K^+ \rightarrow \mu^+\nu$ events with $m^2_{miss}(RICH)$ lower (greater) than 0.01 GeV^2/c^4. $K^+ \rightarrow \pi^+\pi^0$ and $K^+ \rightarrow \mu^+\nu$ factors are applied on a run-by-run basis to take roughly into account effects from different beam intensity. These factors should include also the effects of the radiative tails, for which more studies are in progress. Here photon rejection (particle ID) in $K^+ \rightarrow \pi^+\pi^0$ ($K^+ \rightarrow \mu^+\nu$) are assumed independent of the kinematic cuts defining the signal regions. The very similar shapes of the m^2_{miss} distribution of $K^+ \rightarrow \pi^+\pi^0$ events before and after photon rejection support this hypothesis (see Section 7.8).

The estimated backgrounds in the signal regions are:

$$N^{exp}_{\pi\pi} = 0.024; \ N^{exp}_{\mu\nu} = 0.011; \ N^{exp}_{\pi\pi\pi} = 0.017. \tag{7}$$

MC studies are on-going to assess the $K^+ \rightarrow \pi^+\pi^-e^+\nu$ background. Previous studies [6] showed that this background is lower than that from $K^+ \rightarrow \pi^+\pi^+\pi^-$. Backgrounds from other decay modes are considered negligible in this document. More detailed studies are in progress.

Background from K^+ early decays discussed in Section 7.3 is evaluated using MC simulation. The number of expected events passing the selection is below 10% of the signal for a kaon mis-matching probability of 2.5% (Section 7.2). More studies on this specific background are on-going.

Backgrounds from inelastic interactions in GTK3 are assumed negligible at this level of sensitivity.

The estimation of the background in control regions around the signal ones is not performed due to the small data set so far. For larger samples of data a blind analysis for both signal and background is planned.

The total background is a factor four larger than expected. The suppression of the $K^+ \to \pi^+\pi^+\pi^-$ background is not finalised yet because the detector capabilities are not fully exploited. Preliminary studies already indicate the possibility to reduce this background further by a factor between five and ten. The excess of background from $K^+ \to \pi^+\pi^0$ and $K^+ \to \mu^+\nu$ is due mainly to the kinematical tails, a factor three larger than expected (Section 7.5), and to the μ^+ suppression, 1.5 less efficient than predicted. Studies are on-going to reduce these backgrounds, showing substantial rooms for improvements from kinematic reconstruction and optimization of the analysis method.
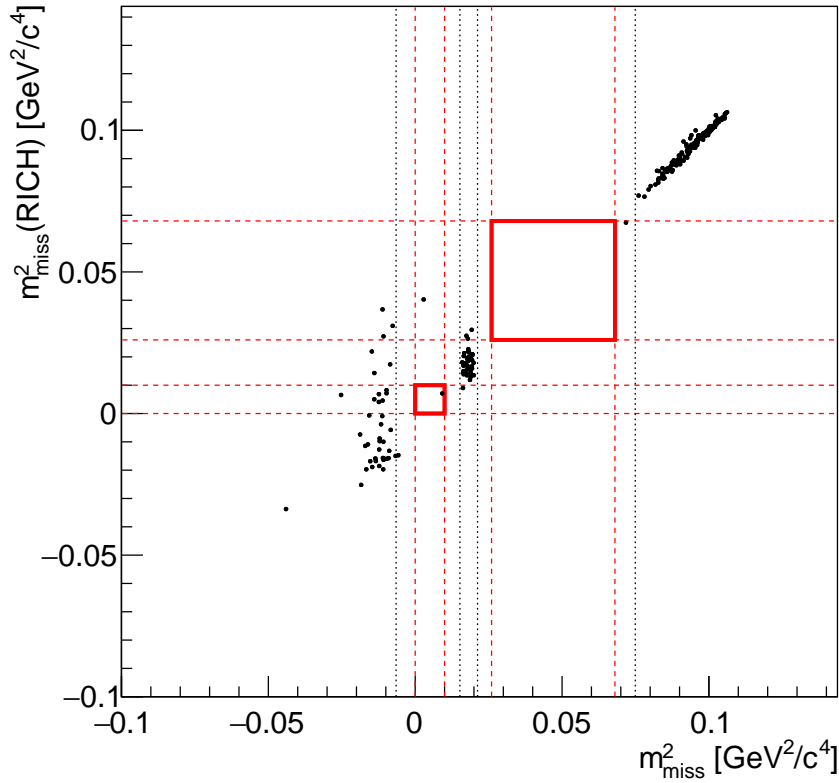
Figure 14: Distribution in the $(m^2_{miss}(RICH), m^2_{miss})$ plane of PNN triggered events passing the $\pi\nu\nu$ selection, except for the cut on $m^2_{miss}(No-GTK)$ (Section 7.5). Signal regions (red tick boxes) and lines defining the background regions (light dashed lines) are drawn. The event apparently left in region 1 has $m^2_{miss}(No-GTK)$ outside the signal region.

7.13   Result and Summary

No events are found in the three-dimensional $(m^2_{miss}, m^2_{miss}(RICH), m^2_{miss}(No-GTK))$ signal regions defined in Section 7.5 after the analysis of about 2.3×10^{10} K^+ decays in a 60 m fiducial region (5% of the available 2016 statistics), in agreement with the expectations for signal and background. For illustration Figure 14 shows the events in

the $(m^2_{miss}(RICH),\ m^2_{miss})$ plane passing the $\pi\nu\nu$ selection, except the conditions on $m^2_{miss}(No\ GTK)$. The only event inside region 1 has $m^2_{miss}(No\ GTK)$ outside the signal region. Taking into account the signal acceptance (Section 7.11), the single event sensitivity turns out to be below 10^{-9}. The analysis on the full 2016 data set is in progress.

8 Exotic physics searches at NA62

The high-intensity setup, trigger system flexibility, and detector performance – high-frequency tracking of beam particles, redundant PID, ultra-high-efficiency photon vetoes – make NA62 particularly suitable for searching for new-physics effect from different scenarios. In the present section, we will outline one of the most advanced searches in this sector, while briefly discussing status and outlook for several other "exotic" physics searches.

8.1 Search for an invisible vector boson from π^0 decays

One of the possible extensions of the SM aimed at explaining the abundance of dark matter in our universe predicts a new $U(1)$ gauge-symmetry sector, with a vector mediator field A' named "dark photon." In a simple realization of such a scenario [7, 8], the A' field A would (feebly) interact with the SM photon through a "kinetic mixing" lagrangian,

$$\epsilon A^{\mu\nu} F_{\mu\nu}, \tag{8}$$

where $F_{\mu\nu}$ represents the e.m. field and ϵ is a small parameter. In a general picture, the above lagrangian might be accompanied by further interactions, both with SM matter fields and with a secluded, hidden sector of possible dark-matter candidate fields. If these are lighter than the A', the dark photon would decay mostly "invisibly", so that a missing-energy signature might reveal its presence.

In this study, an A' search is performed, with A' escaping detection from the decay chain

$$K^+ \to \pi^+\pi^0 \text{ with } \pi^0 \to A'\gamma, \tag{9}$$

where

$$\mathrm{BR}\left(\pi^0 \to A'\gamma\right) = 2\epsilon^2 \left(1 - \frac{m_A^2}{m_{\pi^0}^2}\right)^3 \times \mathrm{BR}\left(\pi^0 \to \gamma\gamma\right) \tag{10}$$

Exploiting extreme photon-veto capability and high resolution tracking while sustaining a high-rate environment makes this analysis synergic with and parasitic to the $K^+ \to \pi^+\nu\bar{\nu}$ measurement.

8.1.1 Analysis strategy and data reduction

The analysis is based on about 1.5×10^{10} K^+ decays in 60 m fiducial region from triggered samples used for the $\pi\nu\nu$ analysis: the PNN L0 trigger for signal search and the minimum-bias control trigger to normalize signal counts to the π^0's produced.

Events with one charged daughter particle are required: exactly one spectrometer good-quality track geometrically associated to a candidate in the NA48-CHOD is reconstructed, with the same requirement as for the $\pi\nu\nu$ analysis. The track has to be

associated in space and time with exactly one upstream beam track, reconstructed with the GTK detector. Tight requirements are applied for the association, in order to minimize the effect of kinematic tails in the reconstruction: the matching time difference should be less than 400 ps and the spatial distance should not exceed 5 mm. The longitudinal coordinate of the beam-to-daughter vertex position should lie in the interval $115 < z_v < 165$ m, thus reducing any reconstruction complication due to the early decays discussed in Sec. 7.3. As for $\pi\nu\nu$ analysis, the track momentum should lie in the range

$$15 < p_\pi < 35 \text{ GeV/c}, \tag{11}$$

thus ensuring at least 40 GeV of energy for the π^0.

The beam particle is identified as a charged kaon from its association in time (to within 2 ns) with a candidate from the KTAG detector with signals in five or more octants. The beam particle momentum reconstructed by the GTK, p_K, should lie in the range

$$72 < p_K < 78 \text{ GeV/c}, \tag{12}$$

to be consistent with the beam momentum distribution.

In order to achieve pion identification, the daughter track is associated in time with a single ring from the RICH consistent with the track position and direction, and in time and space with energy deposits from the downstream calorimeter system (LKr, MUV1, and MUV2 calorimeters), while having no hit associated to within 3 ns and 15 cm from the muon-veto detector MUV3 (this takes into account the effect of multiple scattering). Information from LKr, MUV1, and MUV2 is combined like in the $\pi\nu\nu$ analysis (Sections 7.6 and 7.7), pushing μ-to-π misidentification to the final level of 10^{-7}.

Given the above particle identification, the squared missing mass evaluated from beam and daughter particles is required to be around the π^0 mass peak:

$$0.013 < (P_K - P_\pi)^2 < 0.023 \text{ GeV}^2/\text{c}^4. \tag{13}$$

For the present analysis, the total number of events with control trigger in the above missing-mass window is $518\,444$. This has to be corrected for the trigger downscaling factor, 400, to obtain the expected number of $K^+ \to \pi^+\pi^0$ events to be selected in the sample, $n_{\pi^0} \sim 20710^6$.

Stringent requests are applied to identify the decay chain in equation 9:

- No signal from the LAV and SAV systems must be present with a time consistent with the reference time (T0) evaluated using the RICH, KTAG, and GTK information;

- Exactly one LKr cluster of energy $E_\gamma > 1.5$ GeV is required at least 30 cm away from the pion impact point, with time consistent with the T0; it is assumed to be due to a photon originating from the charged vertex;

- The total missing momentum evaluated from kaon and pion momenta and from the photon cluster should extrapolate to the LKr calorimeter, thus ensuring an optimal photon detection efficiency;

- No activity in the LKr should be found corresponding to auxiliary clusters of total energy above 1 GeV around the expected missing momentum extrapolated point;

- No hit in time from the RICH detector should be found in addition to those reconstructing the pion Cherenkov ring, thus minimizing the contribution from upstream photon conversions in the straw chambers and RICH vessel materials;

- The expected impact point of the missing momentum at the LKr should be far from the pion and photon clusters by more than 20 cm, thus minimizing the condition of energy sharing.

Given the kaon, pion, and photon momenta, the squared missing mass

$$M^2_{\mathrm{miss}} = (P_K - P_\pi - P_\gamma)^2 \tag{14}$$

is expected to peak around the A' mass for the decay (eq. 9) and around zero for the natural background due to $\pi^0 \to \gamma\gamma$ decays with one photon undetected, as shown in Figure 15. Results from MC simulations using various A' masses are superimposed to the expected contribution from $\pi^0 \to \gamma\gamma$ data events in which one photon cluster in the LKr has been fictitiously excluded on the basis of the expected detector inefficiency (measured on data control samples).
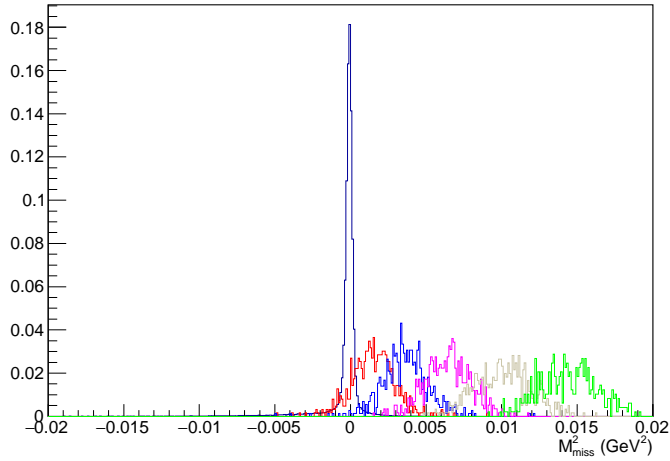
Figure 15: Distribution of the squared missing mass evaluated from one photon and one π^+ from K^+ decays, Eq. 14: data from $\pi^0 \to \gamma\gamma$ events in which one photon is assumed to be undetected according to the expected inefficiency (black line) is compared with the expected spectra from $\pi^0 \to A'\gamma$, for A' masses from 40 to 120 MeV in 20-MeV steps (red to green lines).

After the above criteria, $166\,518$ events are selected, corresponding to a rejection of $\pi^0 \to \gamma\gamma$ single photons at the level of 8×10^{-4}: this is dominated by the loss of few-GeV photons in the LKr, whereas the remaining photons tend to have energy above 30 GeV. This figure is entirely consistent with the overall π^0 rejection power obtained for the $\pi\nu\nu$ analysis, see Sec. 7.8. The signal for A' masses above 70 MeV tends to have photons of energy below 20 GeV. The width of the background peak is due to experimental resolution effects, which are mainly left-right symmetric. This allows a data-driven background estimate, based on the tail with negative missing mass values,

as shown in Fig. 16. For each A' mass, the signal region is defined as a 1.5-standard deviation range around the expected invariant mass peak. Frequentistic 90% confidence intervals have been determined, taking into account the uncertainties of signal efficiency from MC determination, and the statistical uncertainties of data counts and background expectations. No statistically significant excess has been detected and upper limits have been computed on the number of signal events, $n_{\rm sig}$.
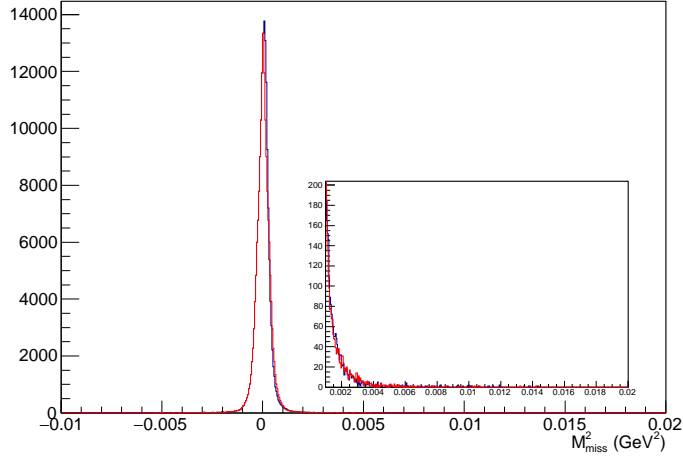
Figure 16: Distribution of the squared missing mass evaluated from one photon and one π^+ from K^+ decays, Eq. 14: data from events in which only one photon is detected. In the region of positive values of squared missing mass, the data plot (black line) is compared with the expected background obtained from the negative tail (red line). In the inset, the region relevant to the A' signal is zoomed.

The ratio of the number of signal events to the number of π^0's counted in the sample allows a determination of the ϵ coupling parameter:

$$\frac{n_{\rm sig}}{n_{\pi 0}} = \frac{{\rm BR}(\pi^0 \to A'\gamma)}{{\rm BR}(\pi^0 \to \gamma\gamma)}\varepsilon_{\rm sel}\varepsilon_{\rm trg}\epsilon_{\rm mass}, \tag{15}$$

where the ratio of selection and trigger efficiency with respect to the normalization sample have been estimated using a combination of data-driven and MC methods and the $\epsilon_{\rm mass}$ correction accounts for the mass range used when determining the signal counts.

8.1.2 Summary and result

Upper limits at the 90% CL in the plane of the coupling (ϵ) versus the A' mass (M_A) are shown in Fig. 17: the limit obtained (black curve) is compared with that obtained when assuming equal counts for data and background (red curve).

Results indicate that the statistical capability of NA62 allows an improvement on previous recent results. A more refined background evaluation might be needed: this point will be clarified after analysis of a larger data sample. It has to be underlined that the technique here used is totally independent with respect to the other recent results. In the picture, the label "$K \to \pi\nu\nu$" refers to a model-dependent limit from the

Brookhaven E787/E949 experiments. The red band indicates the region favoured by the present discrepancy of experimental result and expected value of the anomalous magnetic moment of the muon: A' discovery in the red region would clarify the $(g-2)_\mu$ puzzle, while the deep blue region is excluded by the agreement of $(g-2)_e$ expectation with the experimental measurement.
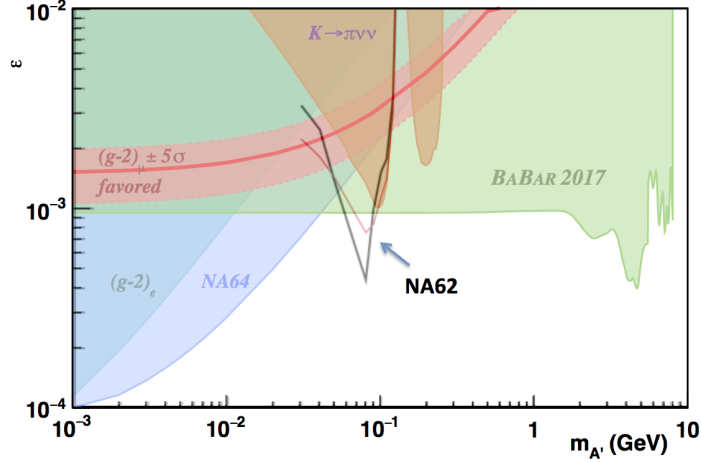
Figure 17: 90%-CL upper limit in the ϵ^2 vs M_A plane, from Eq. 15. In black, the upper limit obtained is compared to that with equal data and background counts. Upper limits from NA62 are compared to main other results from search of A' invisible decays. The picture is adapted from [9]. See comments in the text.

8.2 Other exotic searches in progress

8.2.1 Long-lived exotic particles

The NA62 beam intensity corresponds to a large number of proton interactions in the T10 target: one nominal year of data taking corresponds to a few 10^{18} protons on target (POT), which in turn corresponds to 10^{18} mesons with the following ratios per species, $\pi^0/\eta/\eta'/\Phi/\rho/\omega = 6.4/0.68/0.07/0.03/0.94/0.95$, and to $\sim 10^{15}$ charmed mesons. The mesons, in turn, might decay to exotic particles (dark photons, heavy neutral leptons). These are expected to have feeble interactions with SM fields and therefore to be extremely long lived: an exotic particle produced in the target might reach the NA62 sensitive volume, decaying therein.

Dedicated triggers have been implemented in order to search for two-body leptonic decays of dark photons or heavy neutral leptons. These are indicated as "exotic" in Table 1. The strategy is to require two charged tracks in the CHOD, and to enforce at L1 the presence of a negative track, as discussed in Sec. 3.2, thus rejecting most of the background from charged kaon decays.

Sensitivity projections have been performed, including trigger efficiency and simple selection criteria. Under the assumption of complete background rejection, we expect to improve on past results after the analysis of one full nominal year of data. At the moment,

background rejection has been proven up to 10^{15} POT for di-muon final states, while a few 10^{17} POT acquired in 2016 are under analysis.

8.2.2 Dedicated runs for axion-like particle search

We can search for Axion-like particles predominantly coupled to two photons and produced in the upstream copper collimator through a Primakov process. For this search, two dedicated runs of a few hours each have been taken in November 2016. In these runs the T10 target was removed and the P42 proton beam was dumped entirely into the "TAX collimators."

Both runs in total amounted to 17 hours and were taken at a point in time when beam quality was not optimal for $\pi\nu\bar{\nu}$ data taking (LHC Ion filling). If backgrounds can be sufficiently rejected, the data taken so far could be enough to slightly improve the sensitivity for these particles beyond existing limits in the region of a few tens of MeV in a so-far untested region of two-photon coupling. For the analysis of these runs, the data reconstruction has recently been adapted to facilitate background rejection: in contrast to the standard algorithm, tracks of momenta much higher than the nominal momentum of the hadron beam as well as tracks with large angles with respect to the beamline are reconstructed. This is possible because of the lower total rate of these dedicated runs with respect to standard data taking and should allow a better rejection of beam halo tracks.

9 Rare and forbidden decays Analysis

9.1 Multi-track data samples

As for the $K^+ \to \pi^+\nu\bar{\nu}$ decay, the NA62 sensitivities to the branching ratios of most rare and forbidden decays of the K^+ and π^0 are in the range 10^{-11} to 10^{-12} (the main source of neutral pions being $K^+ \to \pi^+\pi^0$ decay). Along with the advanced particle identification and background suppression capabilities and excellent resolution, this opens a way for a programme of rare decay measurements and searches for forbidden decays at record precision. Dedicated electron multi-track, muon multi-track and di-muon trigger chains designed to collect a wide range of multi-track K^+ decays have been operating simultaneously with the main $K^+ \to \pi^+\nu\bar{\nu}$ trigger since July 2016 (Section 4 and Table 1). The L0 stage of these trigger chains is based on coincidences of multiplicity signals from RICH, NA48-CHOD and MUV3 detectors and the total energy deposition in the LKr calorimeter, while the principal component of the high-level trigger is the requirement of reconstructing a negative track in the STRAW. Improved versions of these trigger chains, optimized using the feedback from the analysis of 2016 data, will be in operation in 2017 and 2018.

The rare decay programme includes measurements of $K^+ \to \pi^+\ell^+\ell^-$, $K^+ \to \pi^+\gamma\ell^+\ell^-$ ($\ell = e, \mu$), $K^+ \to \pi^+\pi^0 e^+ e^-$ and $\pi^0 \to e^+ e^-$ processes. The forbidden decays under consideration include lepton flavour and lepton number violating decays (LFV, LNV) like, $K^+ \to \pi^-\ell_1^+\ell_2^+$, $K^+ \to \ell_1^-\bar{\nu}\ell_2^+\ell_2^+$ ($\ell_{1,2} = e, \mu$), $K^+ \to \pi^+\mu^\pm e^\mp$ and $\pi^0 \to \mu^\pm e^\mp$ decays, as well as $K^+ \to \pi^+\pi^+\ell^-\nu$ decays violating the $\Delta S = \Delta Q$ selection rule.

Both data from sample A and B defined in Section 4 are suitable for the rare decays
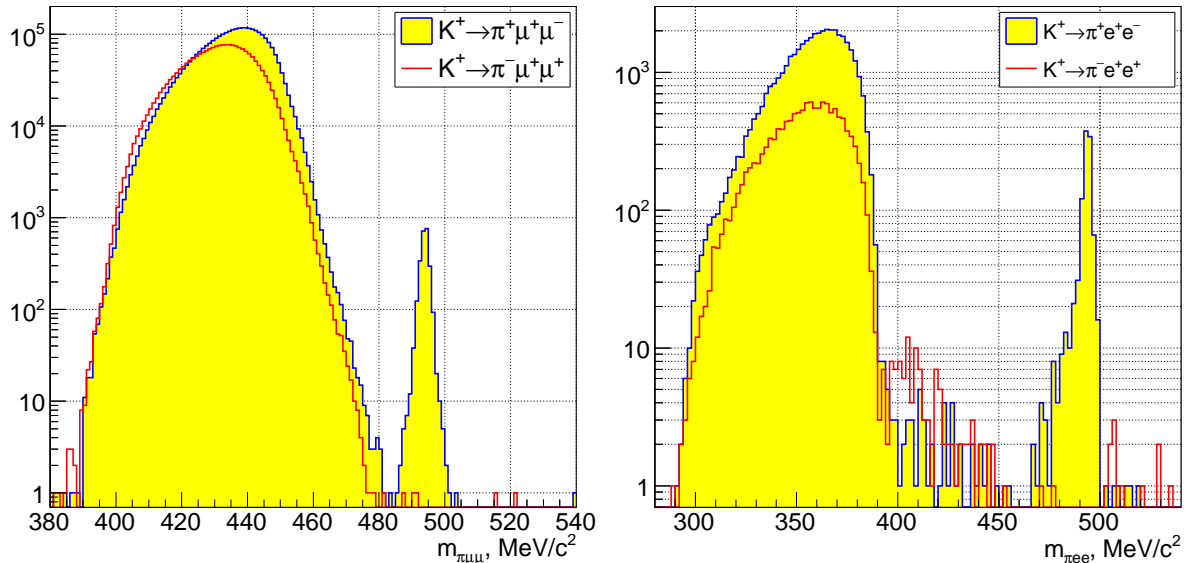
Figure 18: Reconstructed $\pi\ell\ell$ mass spectra obtained from a partial 2016 data sample with selections for the rare decays $K^+ \to \pi^+\ell^+\ell^-$ and forbidden LNV decays $K^+ \to \pi^-\ell^+\ell^+$.

programme. For what concerns the already reprocessed sample A, the di-muon trigger has been in operation without downscaling for the whole period, while the effective downscaling factors of the electron multi-track and muon multi-track triggers were about 3 and 5, respectively. Several analyses based on this partial data sample are in progress. As an example, the reconstructed $\pi\ell\ell$ mass spectra obtained with a basic monitoring selection for rare decays $K^+ \to \pi^+\ell^+\ell^-$ with branching ratios of $\mathcal{O}(10^{-7})$ and LNV decays $K^+ \to \pi^-\ell^+\ell^+$ are shown in Fig. 18. The numbers of $K^+ \to \pi^+\mu^+\mu^-$ and $K^+ \to \pi^+e^+e^-$ candidates observed are 2.4×10^3 and 1.0×10^3, respectively, which are about 75% and 10% of the largest samples obtained so far by the NA48/2 and BNL E865 experiments [10, 11]. The backgrounds are well below 1%, which is smaller than or similar to those reported by previous experiments. The sensitivities to the branching ratios of the LNV decays $K^+ \to \pi^-\ell^+\ell^+$ obtained with this partial sample are at the 10^{-10} level, comparable with the most stringent previous upper limits [12, 13].

9.2 Minimum bias data samples

Dedicated minimum bias data samples have been collected at low beam intensity in 2015 and early 2016 using loose NA48-CHOD and MUV3 based L0 trigger conditions. Additionally, a downscaled control sample is recorded at high intensity with the NA48-CHOD trigger as part of the regular high intensity $K^+ \to \pi^+\nu\bar{\nu}$ data taking. These samples offer a number of opportunities to test various 'dark sector' models, as well as to measure rare K^+ decays which are difficult to trigger on selectively.

The 'dark sector' physics programme includes searches for $K^+ \to \pi^+X$, $K^+ \to \ell^+X$, $K^+ \to \ell^+\nu X$ and $\pi^0 \to \gamma X$ decays, where X is a new particle (which is either invisible or decays into SM particles). These searches could lead to discoveries of a dark photon, axion, inflaton or heavy neutral leptons (HNL), or to obtain non-trivial limitations on their phase space. The sensitivity of these analyses is generally determined by the background conditions rather than by integrated beam flux, which makes NA62 competitive even with
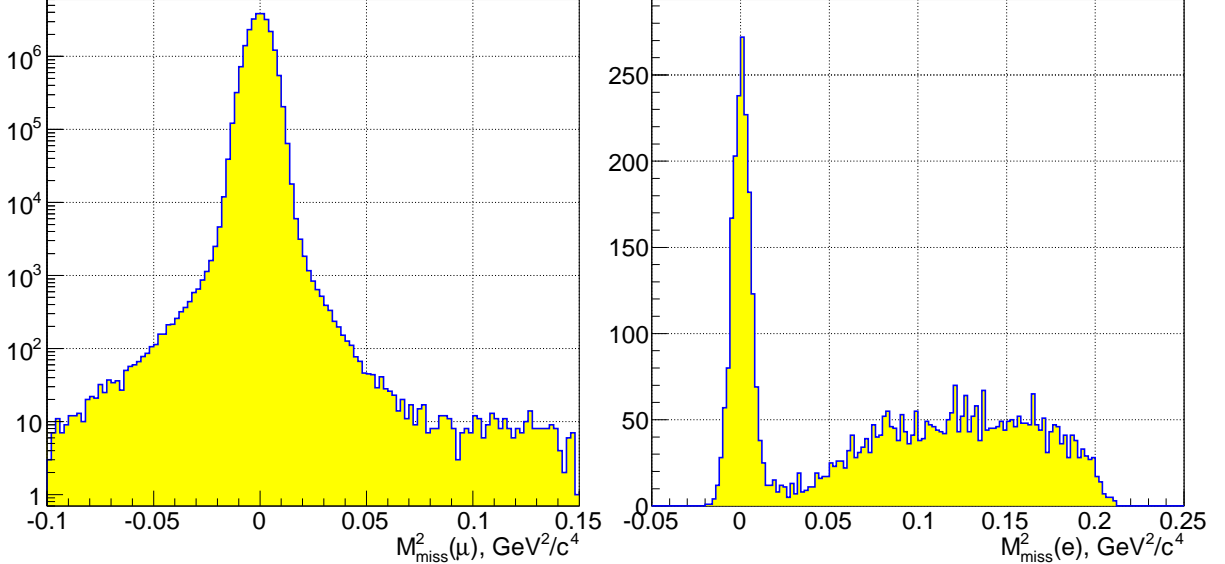
Figure 19: Squared missing mass spectra of the $K^+ \to \mu^+\nu$ (left) and $K^+ \to e^+\nu$ (right) decays reconstructed from 2015 minimum bias data. The backgrounds in the regions of large missing mass are low, leading to record sensitivities to HNL production.

small data sets thanks to the hermeticity of the charged track and photon veto. The rare kaon decay programme with the minimum bias data includes measurements of rare decays $K^+ \to \ell^+\nu\gamma$ and $K^+ \to \pi^+\gamma\gamma$.

A minimum bias data sample containing 1.2×10^4 SPS spills corresponding to about 10^9 kaon decays in the 75 m long fiducial decay volume collected at low beam intensity (below 1% of the nominal one) on 16–20 October 2015 has been reprocessed, and several analyses based on this data set are in progress. These studies will be extended to additional minimum bias data samples, and some of them possibly to regular samples collected with the $K^+ \to \pi^+\nu\bar{\nu}$ trigger.

One of the more advanced analyses is the search for HNL production in kaon decays: $K^+ \to \ell^+ N$ ($\ell = e, \mu$). The existence of a HNL in the $\mathcal{O}(1~\text{GeV})$ mass range is predicted by the neutrino minimal Standard Model (νMSM), explaining dark matter and baryon asymmetry of the universe in a way consistent with the results of neutrino oscillation experiments [14]. The advantage of production searches is that HNL production is decoupled from its decay; as a consequence the sensitivity to the $|U_{\ell 4}|^2$ mixing parameter increases linearly with the integrated beam flux, in contrast to the square-root dependence for a generic beam dump experiment. The search for $K^+ \to \ell^+ N$ decays with the 2015 data aims to put limits on the parameters of the extended neutrino mixing matrix in $|U_{\mu 4}|^2$ (in the HNL mass range 250–370 MeV/c^2) and $|U_{e4}|^2$ (in the HNL mass range 200–450 MeV/c^2). The missing mass spectra of events with single leptons in the final state are displayed in Fig. 19. The background in the HNL signal region at high missing mass is low (in particular, in comparison with the 2007 data collected using the NA48 detector which lacked hermeticity [15]). The expected sensitivities to $|U_{\ell 4}|^2$ are at the 10^{-7} level over most of the above HNL mass ranges, improving the existing limits from production searches by an order of magnitude.

10 Publications and Analysis of older data

Since the last NA62 SPSC review in April 2016, the collaboration has completed the publication of two physics analyses based on older data sets recorded by NA48/2 (2003-2004) and by NA62 (2007) and prepared a reference publication on the NA62 detector:

- NA62 Collaboration: The beam and detector of the NA62 experiment at CERN, being submitted to JINST [1];

- NA62 Collaboration: Measurement of the *pio* electromagnetic transition form factor slope, published in Physics Letters B [16];

- NA48/2 Collaboration: Search for Lepton Number Violation and Resonances in $K^{\pm}$ to $\pi\mu\mu$ Decays, published Physics Letters B [12].

More analyses have been approved as preliminary results and are presented at Conferences while draft papers are being prepared for review within the corresponding Collaborations and timely publication.

- Search for Heavy Neutrinos in $K^+ \rightarrow \mu^+\nu$ Decays (NA62, 2007 Data);

- Precision measurement of the Kl3 Form Factors (NA48/2, 2004 Data);

- First observation and study of the $K^{\pm}$ to $\pi^{\pm}\pi^0 e^+ e^-$ decay (NA48/2, 2003-2004 Data);

- Model independent measurement of the $K^{\pm}$ to $\mu^{\pm}\nu e^+ e^-$ decay (NA48/2, 2003-2004 Data).

The collaboration is actively contributing to major International Conferences and topical Workshops with NA62 Detector contributions and recently published or preliminary physics results from NA62 and NA48/2 data analyses. In the past year (April 2016 to April 2017), the collaboration speakers presented 63 talks and 3 poster to Physics Conferences and 19 talks and 5 posters to Instrumentation Conferences. More contributions are already foreseen in future 2017 Conferences.

References

[1] The NA62 Collaboration, submitted to arXiv and JINST.

[2] R. Veenhof, GARFIELD, http://garfield.web.cern.ch/garfield.

[3] C. Patrignani *et al.* (Particle Data Group), Chin. Phys. C, **40** (2016) 100001.

[4] A.J. Buras, D. Buttazzo, J. Girrbach-Noe and R. Knegjens, JHEP **1511** 33 (2015).

[5] NA62 Technical Design Document NA62-10-07;
    https://cdsweb.cern.ch/record/14049857.

[6] G. Ruggiero (NA62 Collaboration), *PoS KAON* **13** 032 (2013).

[7] L. Okun, Sov.Phys.JETP 56 (1982) 502.

[8] B. Holdom, Phys.Lett. B166 (1986) 196.

[9] J. P. Lees *et al.* [BaBar Collaboration], arXiv:1702.03327 [hep-ex].

[10] J.R. Batley *et al.*, Phys. Lett. **B697** (2011) 107.

[11] R. Appel *et al.*, Phys. Rev. Lett. **83** (1999) 4482.

[12] J.R. Batley *et al.*, Phys. Lett. **B769** (2017) 67.

[13] R. Appel *et al.*, Phys. Rev. Lett. **85** (2000) 2877.

[14] T. Asaka and M. Shaposhnikov, Phys. Lett. **B620** (2005) 17.

[15] C. Lazzeroni *et al.*, Phys. Lett. **B719** (2013) 326.

[16] C. Lazzeroni *et al.*, Phys. Lett. **B768** (2017) 38.